Assessing spatio-temporal variability of melt–refreeze patterns in firn ~~volume scattering~~ over Greenland with satellite ~~altimeters~~CryoSat-2

Weiran Li [1], Stef Lhermitte [2, 1], Bert Wouters [1], Cornelis Slobbe [1], Max Brils [3, 5], and Xavier Fettweis [4]

[1]Department of Geoscience and Remote Sensing, Delft University of Technology, Delft, the Netherlands
[2]Department of Earth & Environmental Sciences, KU Leuven, Leuven, Belgium
[3]Institute for Marine and Atmospheric Research, Utrecht University, Utrecht, the Netherlands
[4]Spheres research unit, Geography, University of Liège, Liège, Belgium
[5]Geography and Environmental Sciences Department, Northumbria University, Newcastle upon Tyne, UK

Correspondence: Weiran Li (w.li-7@tudelft.nl)

Abstract. In recent decades, satellite radar altimetry has been widely used to assess volume changes over the Greenland Ice Sheet. Especially, melt events result in drastic changes in volume scattering of firn, which induces a pronounced change in parameters derived from radar altimetry. Due to the recent and increasingly frequent melt events over Greenland, the impacts of these events on the firn condition i.e. formation of ice lenses and reduction of firn air content, need to be better understood. This study therefore exploits the ability of long-term CryoSat-2 data in indicating changes in firn volume scattering, in order to assess the spatio-temporal firn condition variations in Greenland. More specifically, this study utilises the leading edge width (LeW) parameter derived from CryoSat-2 Low Resolution Mode, which has been proven to be the parameter most sensitive to changes in volume scattering, and assesses its variation between ~~January 2011 and August 2021.~~ September 2010 and September 2024. With a combined analysis of remote sensing observations, in situ observations and outputs from regional climate models, our study demonstrates that the LeW drop induced by extreme melt events in the interior of Greenland experiences a gradual recovery, which can potentially be explained by new snow deposition. However, in many high-elevation regions of Greenland where firn layers were originally dry, due to the recently recurring extensive melt, the firn volume scattering does not fully recover to the original state before the 2012 melt, indicating a long-lived increase in Greenland's firn density in a changing climate. Finally, our study also confirms the capability of using radar altimeter data to monitor changes in volume scattering properties of firn in the long-term.

1 Introduction

Over the recent decades, the Greenland Ice Sheet has experienced a notable increase in the frequency and intensity of melt events (Tedesco et al., 2011, 2013; Nilsson et al., 2015; Tedesco et al., 2016; Tedesco and Fettweis, 2020). These events are particularly prevalent in low-elevation regions, where they contribute to runoff towards the ocean. This runoff negatively impacts the surface mass balance ~~(SMB)~~ of the ice sheet and may lead to irreversible ice loss and sea-level rise (Lenton et al., 2008; Sasgen et al., 2012). In contrast, at higher elevations, meltwater can infiltrate and refreeze within the porous firn

(Harper et al., 2012). This refreezing process releases latent heat, which accelerates firn compaction and diminishes the firn's capacity to store additional meltwater, consequently speeding up runoff from the ice sheet's interior (van den Broeke et al., 2016; Machguth et al., 2016; Vandecrux et al., 2019). Surface meltwater also drains towards the bedrock through crevasses and moulins, altering basal frictions and ice velocities (Zwally et al., 2002; Sundal et al., 2011; Meierbachtol et al., 2013). Furthermore, studies suggest that the runoff and melt will continue to increase (Vizcaíno et al., 2009; Huybrechts et al., 2011). Therefore, the determination of , underscoring the importance of assessing the impact of melt and refreezing in the firn layer over Greenland has become of utmost importance on Greenland's firn layer for understanding the ice sheet's overall stability and response to climate change (Heilig et al., 2018).

Remote sensing techniques are essential for long-term, spatio-temporally continuous monitoring of melt and refreezing events over the Greenland ice sheet, as Given the limited spatial and temporal coverage of in situ data are sparse in both space and time (Hall et al., 2008; Koenig et al., 2016; Castelao and Medeiros, 2022). Radar and lidar altimetry sensors, primarily (Hall et al., 2008; Koenig et al., 2016; Castelao and Medeiros, 2022), remote sensing techniques are indispensable for assessing this impact. Radar altimetry is one of them, although so far it has mainly been used to measure surface height (changes) (Helm et al., 2014b; Slater et al., 2018), can provide information on melt and refreezing events with much greater coverage. They do this indirectly, as refreezing impacts firn elevation changes (e.g., Helm et al., 2014b; Slater et al., 2018). The underlying principle is based on the fact that over firn-covered regions of the ice sheet—primarily at higher elevations—radar pulses at frequencies commonly used in satellite altimetry penetrate into the firn (e.g., Ridley and Partington, 1988). According to Ridley and Partington (1988) and Davis and Zwally (1993), the penetration depth may range from a few centimetres to several metres, depending on the firn status ((e.g. dry, wet, refrozen; Slater et al., 2019)) and the retracker (Michel et al., 2014; Simonsen and Sører . Consequently, recorded waveforms contain signals from both surface scattering and volume (or subsurface) scattering caused by inhomogeneities within the underlying firn layers. Surface scattering dominates the start of the waveform, while volume scattering becomes predominant beyond the inflection point, where the illuminated surface area becomes constant. The rise of the backscattered power from volume scattering depends on firn parameters, including firn density, firn air content (FAC), and grain size (Vandecrux et al., 2019; Brils et al., 2022), which further influence the altimetry signals through changes in volume and surface scattering(Fahnestock et al., 1993; Adodo et al., 2018; Alley et al., 2018; Larue et al., 2021). (Ridley and Partington, 1988; Va . For example, larger grain radii and higher firn densities lead to a faster increase in backscattered power (i.e., a steeper leading edge) (Ridley and Partington, 1988, Figs. 9, 10). Melt and refreezing events alter firn parameters and form refrozen layers, modifying scattering behaviour and waveform shape. Depending on thickness and density, refrozen layers can substantially reduce radar penetration, diminishing volume scattering. While these changes in waveform shape are observable, attributing them to variations in volume scattering—and thus to changes in firn properties—requires distinguishing them from variations in surface scattering, particularly those driven by surface roughness. Indeed, a decrease in surface roughness also results in steeper leading edges (Ridley and Partington, 1988, Fig. 8).

Various studies have focused on deriving firn properties from the waveform of the returned radar signal in radar altimetry. For example, the European Space Agency (ESA) CryoSat-2 satellite, equipped with a radar altimeter operating at Several studies have employed waveform shape parameters to gain insight into the impact of melt and refreezing on Greenland's firn layer, as

well as to estimate the bias in radar altimeter-derived elevations caused by radar penetration into the firn. Nilsson et al. (2015), for example, used Ku-band (13.575 GHz) ~~frequency, has been employed~~ altimeter data acquired by CryoSat-2 to track the formation of ice lenses following melt events~~(Nilsson et al., 2015), to understand~~. Simonsen and Sørensen (2017) explored the same data to investigate the impact of volume scattering properties on ~~height estimations (Simonsen and Sørensen, 2017), and to derive surface snow properties such as roughness and density (Scanlan et al., 2023).~~ elevation estimates. Both Nilsson et al. (2015) and Simonsen and Sørensen (2017) showed that a large leading edge width (LeW) is ~~an indicator~~ indicative of volume scattering of the signal in the upper parts of the firn, while Nilsson et al. (2015) in particular observed the impact of the 2012 Greenland melt event and its subsequent refreezing on ~~the parametersderived from radar waveforms~~waveform-derived parameters, including LeW, trailing edge slope (TeS) and peakiness, backscatter intensity, and height. The Simonsen and Sørensen (2017) study indicated that within the region of the Greenland Ice Sheet covered by Low Resolution Mode (LRM) ~~coverage,~~ data (i.e., the LRM zone), LeW could be effectively used to correct for ~~height~~ elevation biases caused by volume scattering. ~~Furthermore, Scanlan et al. (2023) developed a model using~~ In addition to waveform shape parameters, other radar altimeter-derived variables have also been utilised to infer firn properties. For instance, Scanlan et al. (2023) leveraged surface echo powers in Ku-band CryoSat-2 and Ka-band SARAL radar waveforms to derive monthly maps of Greenland Ice Sheet's wavelength-scale surface roughness and density ~~of snow in Greenland between~~ between January 2013 and ~~2019. Finally, using data from NASA's Operation IceBridge (OIB) mission, i.e. data from the Multichannel Coherent Radar Depth Sounder (MCoRDS) and Airborne Topographic Mapper (ATM) laser altimeter, Rutishauser et al. (2024) assessed the relation between vertical offsets in the radar surface reflection and the vertical heterogeneity caused by melt events. In addition, although the study was conducted over Antarctica, Michel et al. (2014) analysed the height~~ December 2018. Furthermore, several studies have estimated radar penetration depths by combining radar and laser altimetry data. Michel et al. (2014), for example, analysed the differences between radar (ENVISAT) and laser (ICESat) ~~altimeters~~ altimeter heights over Antarctica to derive Ku-band radar penetration ~~depths~~ biases into firn and compared these height differences with ~~LeW, providing~~ LeWs. The study provides insights into opportunities for similar approaches to study Greenland's firn.

Despite ~~the~~ these advances in using radar altimetry to monitor Greenland's firn ~~, the evaluation of firn properties has been limited to either to periods~~ properties—particularly in assessing the effects of melt and refreezing—existing studies have largely been confined to a period without extensive melt ~~(e.g. January 2013 to January 2019; Scanlan et al., 2023) or small regions (e.g., NEEM site; Nilsson et al., 2015). However, the availability of over~~ (e.g., January 2013 to December 2018; Scanlan et al., 2023), or to the short timeframe immediately following the 2012 melt event (e.g., up to 2014; Nilsson et al., 2015). The impact on the long term, especially following the 2019 melt (Tedesco and Fettweis, 2020), remain insufficiently monitored. The availability of more than a decade of CryoSat-2 data ~~, offers an opportunity for long-term studies of~~ presents a valuable opportunity to address this gap.

The main objective of this paper is to assess the impact of melt and refreezing events on the properties of Greenland's ~~firn scattering properties. Following previous studies, we focus on two self-derived parameters: the LeW and the height difference between~~ upper firn layer, using LeWs derived from CryoSat-2 radar waveforms acquired between 2010 and 2024. To support the interpretation of the results, we complement the assessment by comparing the LeWs with: (i) the surface roughness dataset

derived by Scanlan et al. (2023) to analyse under which circumstances the LeW variation is dominated by surface scattering; (ii) the ArcticDEM standard deviation to assess the impact of macro-scale roughness due to topographic variation on LeW; (iii) laser-radar height offsets obtained by differencing ICESat-2 laser altimeter elevations and CryoSat-2 ~~, which both will be used to provide insights into the volume scatteringof Greenland firn. The LeW is adopted as it is sensitive to volume scattering variations (Legrésy and Rémy, 1997; Nilsson et al., 2015). The height difference between ICESat-2 and CryoSat-2 is used as an indicator of penetration depths, as Ku-band radar has a larger penetration depth than ICESat-2 green light (Michel et al., 2014; Smith et al., 2018).~~

~~Furthermore, recent developments in climate and firn models, such as~~ radar altimeter elevations to gain further insights into volume scattering; and (iv) firn densities and FAC from the Modèle Atmosphérique Régionale (MAR) (Fettweis et al., 2011, 2017; Lambin et al., 2022) and the Firn Densification Model from the Institute for Marine and Atmospheric research Utrecht (IMAU-FDM v1.2G; Brils et al., 2022) ~~, provide spatially and temporally continuous firn property data. By comparing long-term LeW measurements with firn properties from climate and firn models, we~~ to analyse how spatial and temporal variations in firn properties affect the LeW and to improve the interpretation of radar altimeter scattering properties for future research. ~~Additionally, we expect the height difference between laser and radar altimeters to offer further insights into firn volume scattering, complementing the interpretation of LeW time series (Michel et al., 2014). Finally, to understand the LeW variations, we have to understand both volume scattering and surface scattering, which can influence the LeW variations to different extents (Michel et al., 2014; Nilsson et al., 2015). Therefore, we also interpret the LeW variations derived from our study with the help of the results from previous studies, i.e. Scanlan et al. (2023) and Rutishauser et al. (2024).~~

~~The objective of this paper is , therefore, to assess long-term changes over the Greenland Ice Sheet. For this purpose, we present the spatio-temporal variations of LeW between 2011 and 2021 and of the difference between ICESat-2 and CryoSat-2 height estimations between 2019 and 2021 over the interior of Greenland, and to subsequently assess whether such variations can reflect the variations in firn properties by comparing them with variations in modelled firn density and FAC provided by MAR and IMAU-FDM.~~ The paper is organized as follows. The details of data and coverage are described in Section 2. The derivation of LeWs and ~~height~~ elevation differences between ICESat-2 and CryoSat-2 will be detailed in Section 3. Sections 4 and 5 present, analyse and discuss the results. Finally, our main findings and outlook are presented in Section 6.

2 Data

~~This section introduces the datasets used to assess how the~~

2.1 Reference digital elevation model

The ArcticDEM digital elevation model (DEM) is utilized for three purposes: (i) correcting CryoSat-2 ~~time series can indicate the impact of recurrent melt–refreezing on Greenland 's firn, with a focus on time series of LeW derived from~~ elevation estimates for slope-induced errors using the leading edge point-based (LEPTA) correction method (Li et al., 2022), (ii) computing macro-scale surface roughness resulting from topographic variation, and (iii) segmenting the Greenland Ice Sheet into ten

distinct elevation bands for spatio-temporal analysis. These groups include one below 1500 m, eight between 1500 m and 3000 m, and one above 3000 m.

ArcticDEM is constructed from recent stereo satellite imagery (Porter et al., 2023) and has a systematic error of less than 5 m (Noh and Howat, 2015). The model is available at various resolutions, ranging from 2 m to 1 km (Porter et al., 2023). Consistent with Li et al. (2022), we employ the 100 m resolution ArcticDEM for slope-induced error correction in CryoSat-2 ~~, and height difference between ICESat-2 and CryoSat-2. The time series of satellite data are complemented by reference datasets for a comprehensive interpretation of volume and surface scattering variations.~~ elevation estimates, balancing accuracy and computational efficiency compared to the higher-resolution 2 m dataset.

For macro-scale roughness estimation and elevation-based segmentation of the Greenland Ice Sheet, we use the 1 km resolution ArcticDEM. The roughness metric is defined as the standard deviation of elevations within a 10 km $\times$10 km grid. Prior to segmenting the Greenland Ice Sheet in distinct elevation bands, we first average elevations over the same 10 km $\times$10 km grid to ensure consistency with the grid used for firn model output.

2.2 CryoSat-2 observations

CryoSat-2~~LRM data~~'s primary payload, the SAR Interferometric Radar Altimeter (SIRAL), operates in three measurement modes (Wingham et al., 2006):

1. Low Resolution Mode (LRM): analogous to pulse-limited radar altimetry, this mode is used over relatively flat ice sheet regions and the open ocean.
2. Synthetic Aperture Radar (SAR) Mode: utilising coherent echo processing, this mode provides higher-resolution along-track data from sea ice and sea-ice-contaminated ocean surfaces.
3. SAR Interferometric (SARIn) Mode: combining coherent echo processing with interferometry, SARIn delivers high-resolution along-track data along with across-track echo directions, primarily for ice sheet margins.

This study focuses on LRM data acquired over the interior of the Greenland ~~ice sheet provide waveform information which can be further processed to obtain various parameters (Nilsson et al., 2015; European Space Agency, 2019; Meloni et al., 2020). The acquisition period of the CryoSat-2 LRM Baseline D data we use in this study is between January~~ Ice Sheet, specifically using Baseline E data spanning from September 1, ~~2011 and August 31, 2021. The LeW in metres is computed from the normalised waveform as~~2010, to September 30, 2024.

Both LeWs and elevations (h_C) are estimated using the Offset Centre of Gravity (OCOG) retracker (Wingham et al., 1986; Bamber, 1994). The retracker is applied to waveforms that are normalized based on their peak power. The LeW, expressed in metres, is computed as:

$$LeW = \frac{1}{2} c \Delta t (b_{0.99} - b_{0.01}) S_r, \quad (1)$$

where ~~$b_{0.99}$ and $b_{0.01}$~~ $b_{0.95}$ and $b_{0.05}$ are the range ~~bias corresponding to the bins where the normalised~~ bins at which the normalized waveform power equals ~~0.99 and 0.01, respectively(found with linear interpolation),~~ 95% and 5% of the OCOG

amplitude (A_{OCOG}), respectively, determined via linear interpolation. Here, c represents the speed of light, and ~~S_r is the range resolution of~~ Δt denotes the CryoSat-2 ~~LRM. Waveform examples from different regions of interest in different periods. Pixel A and pixel C refer to the highlighted pixels in Fig. 1.~~ LRM waveform sampling interval (3.125 ns). A_{OCOG} is given by:

$$A_{\mathrm{OCOG}} = \sqrt{\sum_{n=n_1}^{n_2} y^4(n) / \sum_{n=n_1}^{n_2} y^2(n)}, \tag{2}$$

where $y(n)$ denotes the normalised power at bin n. The parameters n_1 and n_2 define the range of bins included in the computation, which serves to mitigate the impact of noise typically present at the beginning and end of the waveform (Frappart et al., 2021; L . In this study, n_1 and n_2 are empirically set to 10 and 125, respectively.

The computation results in approximately 4.55×10^7 LeWs over the entire investigated period in total. Monthly mean LeWs are computed on a 10 km$\times$10 km grid. The time series of monthly mean LeW serves as the basis for analysing temporal LeW variations along a simple north-south transect (connecting the NEEM site, Summit Camp and the southernmost locations of the LRM coverage) and conducting a Greenland-wide assessment of LeW variations across elevation bands.

~~Subsequently, we derive height estimations of~~ A total of approximately 4.61×10^7 CryoSat-2 ~~(h_C)from the waveforms using the Offset Centre of Gravity (OCOG) retracker (Wingham et al., 1986; Bamber, 1994; Gommenginger et al., 2010) with a 50% threshold. Such a high 50% threshold corresponds to~~ elevation estimates (h_C) are derived using the OCOG retracker with a 50% threshold. As discussed by Davis (1997), the ~~radar return within the firn and is expected to indicate the volume scattering of~~ half-power point best represents the mean surface elevation (i.e., the mean elevation of the firn–air interface) within the altimeter's pulse-limited footprint, assuming surface scattering dominates the waveform. However, in firn-covered areas, h_C corresponds to an elevation within the firn layer. By comparing h_C to ice sheet elevations from ICESat-2, we obtain laser-radar height offsets as a proxy for the Ku-band ~~radar in the firn layer (Li et al., 2022). To correct for slope-induced errors in the~~ radar penetration depth (see Sect. 3.3).

Based on the results of Li et al. (2022), we chose to apply the LEPTA method to correct h_C ~~height estimation, we use the leading edge~~ for slope-induced errors. The study, which introduced and compared LEPTA against slope- and point-based ~~(LEPTA) method from Li et al. (2022), as it utilises a high-resolution digital elevation model (DEM) and has the advantage to account for impacts of complex terrains~~correction methods using CryoSat-2 LRM data over Greenland in 2019, demonstrated that LEPTA provides stable performance across both flat interior regions and areas with more complex topography when compared to ICESat-2 observations.

~~To demonstrate the typical waveforms under different conditions and the corresponding LeWs , we provide examples of waveforms before (January) and after (July) the extensive 2012 melt event (Tedesco et al., 2013) in different regions of interest in Fig. ??: pixel A corresponds to the vicinity of the NEEM site as studied by Nilsson et al. (2015), where the difference between January and July 2012 shows reduced volume scattering due to the 2012 melt event. Pixel C corresponds to the region with constantly high surface roughness as derived by Scanlan et al. (2023), where a rougher surface typically corresponds to a higher LeW and less pronounced differences before and after the melt, potentially due to the dominant role of surface scattering from a constantly rough surface.~~

~~Finally, the derived LeWs are grouped into grids with two different resolutions. A 50 km×50 km grid is used to observe the variations along a north-south transect, as this resolution both ensures a sufficient division over the interior of Greenland and a sufficient amount of data per month per pixel.A 25 km×25 km grid is adopted when the data from multiple months are aggregated for the analysis. The mean LeW of all points within each pixel is calculated and utilised.~~

2.3 ICESat-2 observations

~~To assess the volume scattering variation of CryoSat-2, we derive the height variation of CryoSat-2 with respect to a reference surface height as a measure for volume scattering properties; the~~ The laser altimeter-derived elevations of the firn-air interface, which are used to calculate a proxy for the Ku-band radar penetration depths, are obtained from the ICESat-2 L3A Land Ice Height (ATL06) product~~Version 5 (Smith et al., 2020) is hence used as the reference surface~~, Version 6 (Smith et al., 2023a). ICESat-2 ~~uses~~ operates the Advanced Topographic Laser Altimeter System (ATLAS) ~~with laser at a~~ that transmits pulses with a wavelength of 532 nm ~~wavelength~~ (Abdalati et al., 2010). The along-track resolution of the ATL06 product is ~~~ 40~~approximately 40 m (Smith et al., 2023b), and ~~the~~ its geolocation bias is less than 10 m (National Snow and Ice Data Center (NSIDC), 2021).

In this study, we ~~use~~ used ATL06 ~~between~~ data from January 1, 2019~~and August 31, 2021 to~~ , to September 30, 2024, to obtain ICESat-2 ~~heights~~ elevations (h_{ICE2}) for each CryoSat-2 point~~(h_C). The ATL06 data do not have a fixed or regularly gridded resolution, therefore we use a natural-neighbour interpolation to obtain ICESat-2 heights (h_{ICE2}) at each~~ . Following the approach described in Li et al. (2022), we compared CryoSat-2 ~~point (h_C)~~elevations acquired in a given month to ICESat-2 elevations from the same month. For each CryoSat-2 point, ~~the~~ we first identify all ICESat-2 points within a 50 ~~m and acquired within the same month are selected for this interpolation. Over a sloping terrain, extra height differences between h_C and h_{ICE2} can be caused by potential topography differences within the 50~~ m ~~distance. To correct for this topography-induced difference, we bi-linearly interpolate (due to the regular resolution) the reference DEM (100 m ArcticDEM) to both the~~ radius. If ICESat-2 points are available in each quadrant surrounding the CryoSat-2 ~~(h_{DEMC}) and~~ point, ICESat-2 ~~(h_{DEMI}) locations; hence, the differences between the~~ elevations are interpolated to the CryoSat-2 location using natural-neighbor interpolation (h_{ICE2}). Otherwise, nearest-neighbour interpolation is applied. The search for ICESat-2 ~~and~~ points within a 50 m radius of each CryoSat-2 ~~heights (Δh) is calculated as~~

$$\Delta h = h_{\mathrm{ICE2}} - h_C - (h_{\mathrm{DEMI}} - h_{\mathrm{DEMC}})$$

~~The spatial distribution as well as the overall probability distribution of Δh between January 2019 and August 2021 are visualised in Fig. 2. However, when the radar altimeter waveform is dominated by surface scattering, a 50 % threshold retracker can still result in an underestimated or negative penetration depth (Davis, 1997). In addition, for the analysis where we compare and interpret the spatio-temporal variations with firn properties, we need to select a valid penetration depth that corresponds to the vertical resolution of the available firn models (i.e., MAR and IMAU-FDM)to ensure a fair comparison. Figure 2 shows that Δh is generally between 0 and 1.5 m on the interior of the ice sheet, therefore this range is used to select valid Δh that can be used as an indicator of volume scattering.~~

Statistics of height difference between ICESat-2 and CryoSat-2 (Δh). (a) is the median Δh per grid cell in a 25 km $\times$25 km grid; the background is the 1 km $\times$1 km DEM from Helm et al. (2014a, b). (b) is the probability distribution function of Δh with percentiles labelled in vertical lines.

2.4 Reference DEM

The ArcticDEM is used to (i) correct the CryoSat-2 LRM height estimations for slope-induced errors with the LEPTA correction method (Li et al., 2022), and (ii) divide the Greenland ice sheet into different elevation groups for the spatio-temporal analysis. The ArcticDEM is constructed from recent stereo satellite imagery (Porter et al., 2023) with a systematic error below 5 m (Noh and Howat, 2015). The ArcticDEM is available in different resolution, ranging from 2 m to 1 km (Porter et al., 2023) . For computational efficiency, we first use the 100 m resolution ArcticDEM to correct for slope-induced errors in deriving CryoSat-2 height estimations (Li et al., 2022). To assess the impact of the topography on the spatial variability of LeWs, we use the 1 km resolution ArcticDEM in the subsequent spatio-temporal analysis due to computational efficiency measurement yields a total of approximately 4.53×10^5 points.

2.4 Firn models

To support the interpretation of the altimeter-derived parameters (LeW and Δh) LeWs and laser-radar height offsets, we use firn density, melt water content (MWC), and firn air content (FAC) from two different regional climate and firn models, : the Modèle Atmosphérique Régional (MAR, Section 2.4.1) and the IMAU Firn Densification Model (IMAU-FDM, Section 2.4.2) respectively.

2.4.1 Modèle Atmosphérique Régional (MAR)

Layered firn densities and melt water meltwater content (MWC) over the study period are obtained from the version 3.12 version 3.14 of the Modèle Atmosphérique Régional (MAR) forced by the ERA5 reanalysis (Fettweis et al., 2017; Lambin et al., 2022) (Fettweis et al., 2017; Lambin et al., 2022; Grailet et al., 2024; Machguth et al., 2024). The MAR outputs have a spatial (horizontal) horizontal resolution of 10 km and a daily temporal resolution, whereas the vertical resolution of the snowpack varies in time between 1 cm close to over depth, from 10 cm near the surface to 5 m at the bottom of the snowpack. The MAR model resolves here the only the upper 20 first metres of snow only and the metres of the snowpack.

We use the time series of modelled firn density profiles to compute the weighted average density of the upper 1.5 m (a threshold based on Fig. 2) is calculated based on the depth of each snow layer thickness. firn column, from the surface to the maximal proxy for Ku-band radar penetration depth. Thickness is used as a weighting factor to account for the model's uneven vertical resolution. The maximal proxy for Ku-band radar penetration depth is empirically determined by analysing the differences between ICESat-2 laser altimeter elevations and CryoSat-2 radar altimeter elevations (see Sect. 3.3).

The firn density profile can be used to infer the amount of provides insights into volume scattering. For example, the presence of a refrozen layer (i.e. a layer with high density; Nilsson et al., 2015; Otosaka et al., 2020) prevents the penetration

~~of the radar signal , hence reduces the~~ (i.e., a layer with high density; Nilsson et al., 2015; Otosaka et al., 2020) prevents radar signal penetration, thereby reducing volume scattering.

The MWC is used to restrict our analysis to non-melt conditions, ~~in order to reduce~~ minimising the impact of meltwater production on Ku-band radar and 532 nm laser measurements. When MWC> 0, meltwater is present in the firn layer, hence the altimeter-derived parameters~~as well as the densities should be excluded. A nearest-neighbour interpolation is performed to identify the MWC values~~ . The MWC value at each CryoSat-2 location is obtained using nearest-neighbour interpolation.

To assess the timing and extent of melt–refreeze patterns, ~~the~~ we use the MAR-derived meltwater production and refreezing outputs ~~of MAR (in the unit of mmWE day^{-1}) are used as~~ (expressed in mmWE day^{-1}) as a reference. To provide insights into volume scattering variations, we adopt the total snow height change (i.e., the snowfall accumulation) from MAR~~is adopted. We calculate the~~ . The accumulated total snow height change is calculated as the sum of daily ~~total snow height change from date of~~ changes from the intensive melt ~~(July 12, 2012; Nghiem et al., 2012) to August 31, 2021.~~ in July, 2012 (Nghiem et al., 2012) to September 30, 2024. The time series of these outputs ~~are~~ is visualised in Appendix A. For consistency with CryoSat-2 time series, we compute monthly averages for density, melt, and refreezing from the daily data. Similarly, monthly snow height changes are computed as the sum of daily changes.

2.4.2 Firn Densification Model (IMAU-FDM)

Alternatively, firn density, MWC, and FAC with a 10-day temporal resolution are obtained from the firn density model IMAU-FDM v1.2G (Brils et al., 2022). ~~It~~ This is a Lagrangian 1D firn model ~~which computes~~ that simulates the evolution of the firn thickness, density, temperature, and water balance. It uses a ~~"bucket method" for computing~~ "bucket method" to compute meltwater percolation into the firn. ~~Its~~ The model's ability to accurately ~~model~~ represent firn properties has been validated in ~~Brils et al. (2022).~~ Brils et al. (2022). At its surface, IMAU-FDM is forced by ~~the output of~~ output from the polar version of the Regional Atmospheric Climate Model (RACMO2; Noël et al., 2018). ~~Results from the model are available between~~ Model results are available from October 1957 ~~and~~ to December 2020. ~~Similarly to~~ As with the MAR data, we ~~(i) masked out all FDM data when the MWC is positive and (ii) averaged the density over the top 1.5 m~~compute the weighted average density of the upper firn column, from the surface to the maximal proxy for Ku-band radar penetration depth.

The FAC ~~is~~ represents the vertically integrated porosity ~~in~~ of the firn (Kuipers Munneke et al., 2015), ~~which is in the unit of metres. While the density is calculated over the first 1.5 m but the FAC is calculated for the~~ expressed in metres. It is computed over the entire firn column ~~. FAC is the total porosity of firn~~and serves as a measure of total firn porosity, indicating the ~~capability of the firnlayer~~ firn's capacity to retain meltwater (Vandecrux et al., 2019). ~~Therefore, we use~~ Although CryoSat-2 signals primarily penetrate the upper firn layers, we leverage the modelled FAC time series to ~~validate whether the~~ assess whether the observed melt–refreeze ~~pattern we aim to observe has a large impact on~~ patterns notably influence broader firn conditions. ~~The application of this dataset is two-fold~~

This dataset serves two main purposes. First, to ~~support the interpretation of LeW time series~~determine whether firn conditions changed considerably during the CryoSat-2 observation period, we use IMAU-FDM firn density and FAC as a reference dataset ~~to compare with both LeW and MAR density monthly time series between~~ for comparison with the monthly LeW time series

from January 2011 ~~and~~ to December 2020. Second, ~~to learn about the most recent changes of Greenland ice sheet with respect to previous decades, we derive a long-term time series (between 1961 and 2020) by computing the yearly average of the~~ a time series of yearly averaged IMAU-FDM density and FAC ~~. In addition, while FAC increases with elevation and can have a large spatial variation, i.e. approximately 0 towards the margins and more than 20 m in the interior of the ice sheet, the juxtaposed FAC over the entire studied area shows pronounced spatial variation and little temporal variation. Therefore, the temporal variation needs to be enhanced with respect to~~ from 1961 to 2020 is used to examine recent changes in the Greenland Ice Sheet in the ~~spatial variation in FAC. For this purpose, we remove the long-term mean of each pixel (using the same grids as the resampled CryoSat-2 LeW) from the time series~~context of previous decades.

2.5 In situ density ~~acquisitions~~profiles

~~Besides the~~ In addition to firn model data, we ~~also use available~~ incorporate various in situ density profiles from ~~Schaller et al. (2016b); Otos~~ Vandecrux et al. (2024) at different locations to ~~show~~ assess the impact of melt events on firn layers. In situ measurements ~~are helpful in providing insights into whether and where refrozen layers persist~~ provide valuable insights into the persistence and distribution of refrozen layers within the Greenland firn, ~~which support~~ supporting the interpretation of ~~the~~ LeW variations. ~~We use~~

We include available and published in situ ~~densities~~ density profiles in our analysis if they meet the following criteria: (i) the acquisition site ~~is~~ falls within the CryoSat-2 LRM coverage; (ii) the acquisition contains the 2012 melt layer ~~to provide~~ or additional melt layers, providing information on the ~~existence~~ presence and depth of refrozen ice layers, (iii) the acquisition is vertically continuous ~~, instead of one~~ rather than a single measurement at a ~~single depth. Therefore, on the one hand, we rely on the 2 m depth firn core densitiesfrom Schaller et al. (2016b)~~ specific depth. It is important to note that, the main reason to contain the 2012 melt year is to provide more sound evidence that the 2012 melt event results in a visible density increase, which can also be observed in the modelled firn densities. This high-density layer is buried in the subsequent years, therefore the recovery in LeW can be eventually observed.

The adopted in situ measurements include profiles collected along a trajectory between NEEM and the East Greenland Ice-core Project (EGRIP) ~~, which were obtained using X-ray tomography in May 2015 (Schaller et al., 2016a) . Due to the dense spatial (horizontal) sampling of the Schaller et al. (2016b) density measurements (22 measurements in total), we select the measurements at NEEM, N2E06 and EGRIP (Schaller et al., 2016a) as representative reference data. On the other hand, we use firn core densities from Otosaka (2020)~~ (Schaller et al., 2016a) and along the Expédition Glaciologique Internationale Au Groenland (EGIG) line ~~, specifically at T12, T19, T30 and T41, which were obtained using stratigraphy in May 2017 (Otosaka et al., 2020)~~(Otosaka et al., 2020). Additional data come from the Summit and Saddle stations (MacFerrin et al., 2022) , the Greenland Traverse for Accumulation and Climate Studies (GreenTrACS; Lewis et al., 2019), ice cores from central west Greenland (CWG; Trusel et al., 2018), and from Vandecrux et al. (2023). The locations and corresponding densities are shown in Fig. 1.

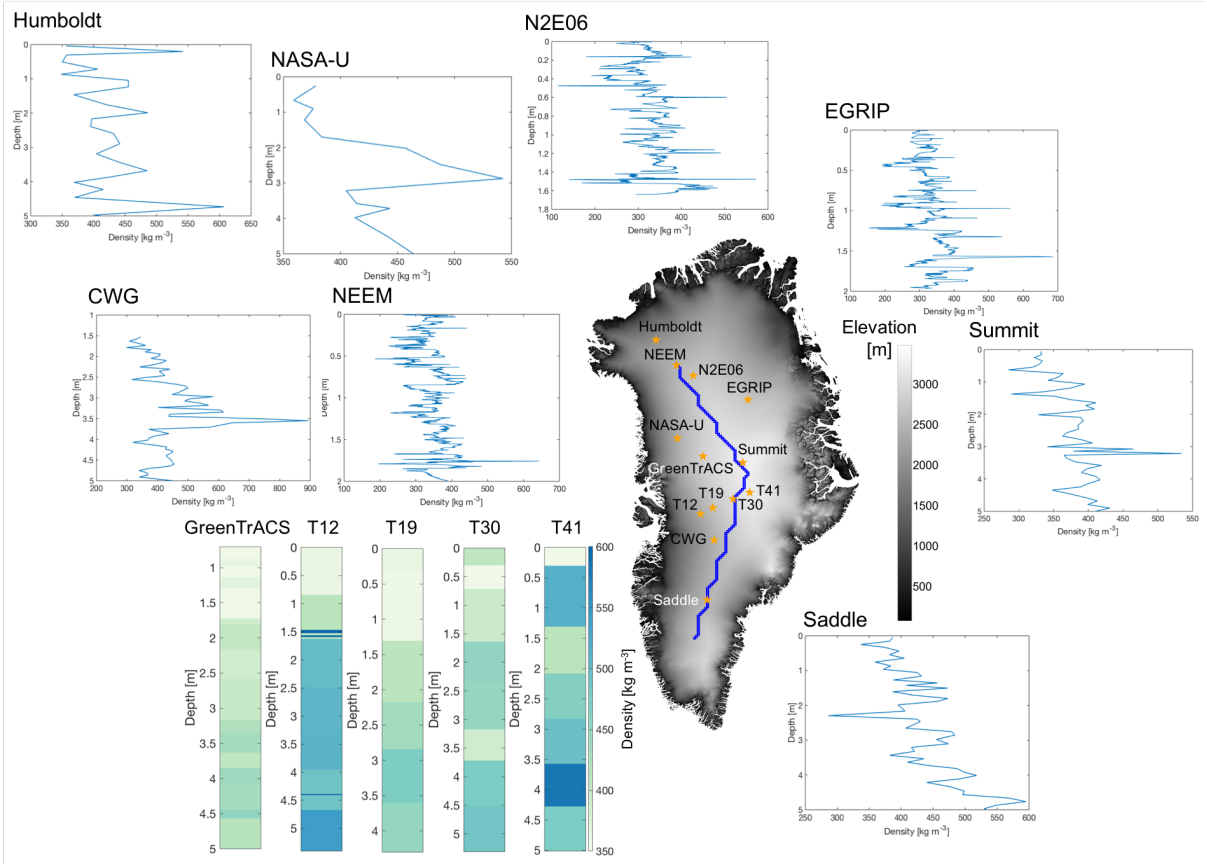

Figure 1. In situ ~~densities~~ density profiles and their measurement locations ~~of measurements: the NEEM, N2E06 and EGRIP measurements are~~ acquired from ~~Schaller et al. (2016b), and the T12, T19, T30 and T41 measurements are from Otosaka (2020)~~ Schaller et al. (2016b); Otosaka (2020); Vandecrux et al. (2024). The background is the 1 km–×1 km ~~DEM from Helm et al. (2014a, b)~~ ArcticDEM. Blue rectangles with a resolution of 10 km×10 km represent the geographic transect ~~of interest~~ used ~~in Section 3~~to present the results.~~Several regions of interest are highlighted with filled blue rectangles, and are taken as examples for a separate time series analysis.~~

2.6 ~~Stratigraphy,~~ Wavelength-scale surface roughness ~~and topography~~data

~~In addition to the modelled firn properties and in situ densities~~ To assess the extent to which changes in LeW can be attributed to variations in wavelength-scale surface roughness, we use the ~~vertical stratigraphy derived from Rutishauser et al. (2024) to understand the formation of melt-induced ice layers. Furthermore, we can analyse the performance and sensitivity of the derived LeW to the melt events by comparing the LeW with the stratigraphy dataset. The stratigraphy is represented by the vertical offsets between the ice surface height obtained by the OIB ATM laser altimeter,~~ wavelength-scale surface roughness dataset derived by Scanlan et al. (2023) from Ku-band CryoSat-2 and ~~the 195 MHz OIB MCoRDS, acquired simultaneously between 2011 and 2019, computed as~~

$$dz = h_{laser} - h_{radar}$$

~~where h_{radar} is the height derived by picking the optimal peaks in MCoRDS surface returns, and h_{laser} is the mean height of all laser observations within MCoRDS' pulse-limited footprint. The obtained dz values correspond with firn stratigraphy (a low dz corresponds to a homogeneous vertical structure). Since dz increases with the vertical heterogeneity of the firn, an increase in dz indicates the formation of refrozen layers (Rutishauser et al., 2024). The dz dataset contains 15.5 million data points with an annual temporal resolution (Rutishauser et al., 2024).~~ Ka-band SARAL radar altimeter data. The data are provided as monthly estimates on a 5 km$\times$5 km grid for the period January 2013 to December 2018. Surface roughness estimates are obtained via the Radar Statistical Reconnaissance (RSR) technique, which statistically characterises the distribution of surface echo powers extracted from individual radar waveforms. The RSR method fits a homodyned K-distribution to the observed echo power histograms to recover relative, dataset-dependent coherent and incoherent powers, which are converted to absolute powers by calibration. Surface roughness is subsequently inferred through inversion using a backscattering model. Spatially, roughness estimates derived from both SARAL and CryoSat-2 LRM reveal a smooth interior becoming progressively rougher toward the margin. The validation of the roughness time series at six locations revealed an annual roughness cycle at one site, with a marked increase in surface roughness during summer, likely associated with surface melting (Scanlan et al., 2023). In order to assess the LeW variations with respect to roughness variations, the roughness dataset is averaged to the 10 km$\times$10 km, consistent with the LeW grid.

~~Additionally, we use the surface roughness dataset derived by Scanlan et al. (2023) to analyse under which circumstances the LeW variation is dominated by surface scattering, since LeW can also be affected by topography and surface roughness (Legrésy and Rémy, 1997; Li et al., 2022). The dataset was created by adopting the Radar Statistical Reconnaissance (RSR) technique in combination with a backscattering model. The temporal coverage of the dataset is between 2013 and 2019 with a monthly resolution.~~

~~As an indicator of topography, the standard deviation of the 1 kmArcticDEM elevations per 50 km$\times$50 km pixel along the north–south transect as well as the standard deviation of ArcticDEM elevations grouped by the aforementioned 10 DEM groups are computed. The ArcticDEM is temporally invariant, therefore only the spatial variation of the standard deviations are presented and analysed.~~

3 ~~Method~~

~~Since LeW variations are driven by both surface and volume scattering, especially melt and subsequent refreezing, we present a qualitative study of the relationship between LeW variations and melt–refreezing events.~~

2.1 ~~Assessment of LeW's ability to indicate scattering variations~~

~~Since LeW variations can be affected by variations in both volume and surface scattering, we first perform a comparison with the available remote sensing data of stratigraphy and roughness (see Section ??) .~~

~~First, to assess the potential of LeW in indicating the~~

3 Methods

3.1 Assessing LeW variability and recovery after the 2012 melt event

This assessment evaluates the spatio-temporal ~~variability in volume scattering, we compare LeWs with dz values derived by Rutishauser et al. (2024). Due to the large amount of dz points, we compute the mean dz values per OIB campaign over the 25 km ×25 km grid consistent to the resampled resolution of LeW .~~ variability of the changes in LeW, with particular emphasis on the recovery of LeW following the extreme 2012 melt event (Tedesco et al., 2013). To this end, we generate a series of maps showing the changes in average LeW over non-melt seasons (October–April) relative to (i) the non-melt seasons of the previous year, and (ii) the baseline period of October 2010 to April 2011. These non-melt season averages are computed using the time series of monthly mean LeW values on a 10 km×10 km grid described in Sect. 2.2. In addition to the maps, we present changes in monthly mean LeW time series—expressed relative to the mean LeW from October 2010 to April 2011—along a geographic transect connecting the NEEM site (Nilsson et al., 2015; Schaller et al., 2016a), Summit Camp, and South Greenland (see Fig. 1). Finally, we ~~mask out grid cells where either dz values or LeWs are not available.~~ examine these changes across ten elevation bands, ranging from below 1500 m to above 3000 m (Section 2.1).

~~Second, we compare the LeW data with the available roughness and topography data as spatio-temporal LeW variations can also be affected by surface scattering, which is composed of surface scattering and topography (Michel et al., 2014; Li et al., 2022) . Therefore, on the one hand, we use the Scanlan et al. (2023) roughness data to represent the wavelength-scale surface roughness. We first resample the Scanlan et al. (2023) data to the 50 km×50 km grid same as the LeW. The time series analysis of LeW and roughness data is two-fold, where we juxtapose LeW and roughness data both (i) along a geographical transect connecting the NEEM site (Nilsson et al., 2015; Schaller et al., 2016a), Summit Camp and South Greenland and (ii) along 10 different averaged elevation bandsbetween 100 m and 3280 m. On the other hand, we also compare the LeW data with the ArcticDEM standard deviation in order to assess the impact of~~

3.2 Assessing the effects of surface roughness (changes) on LeW (changes)

To assess the extent to which changes in LeW can be attributed to variations in surface roughness, time series of both wavelength-scale and macro-scale ~~roughness due to topographic variation on LeW~~ surface roughness covering the same period as the CryoSat-2 LRM data (i.e., September 1, 2010, to September 30, 2024) would be required. Unfortunately, such time series are not available. In the case of macro-scale surface roughness, no time series exist. For wavelength-scale surface roughness, the available data are limited to the period from January 2013 to December 2018 (Sect. 2.6). This constrains the scope of our analysis.

To gain insights into the potential influence of wavelength-scale surface roughness on LeW, we compare time series of monthly mean wavelength-scale surface roughness values with corresponding changes in monthly mean LeW. In both cases, anomalies are computed by subtracting the mean over the January 2013 to December 2018 period. As in the analysis of LeW variability and post-2012 melt recovery, the results are presented along the geographic transect and as averages across ten elevation bands.

3.3 ~~Correlation analysis between LeW and Δh~~

~~Since Δh is a typical indicator of radar altimeter penetration depth (Michel et al., 2014), we compute the correlation between all LeW and Δh estimates to assess to what extent the~~ In addition, we examine the relationship between the absolute values of LeW ~~variation is dominated by the penetration depth hence~~ and surface roughness—both wavelength-scale and macro-scale. These results are also presented along the geographic transect and averaged over the ten elevation bands.

3.3 Assessing the correlation between LeW and laser-radar height offsets

This analysis aims to evaluate the extent to which changes in LeW can be attributed to variations in volume scattering. ~~For this purpose, we adopt the 25 km×25 km grid introduced in Section 2.2. Within each grid cell, the Pearson correlation coefficients are computed between LeW~~ We assess this indirectly by examining the correlation between time series of monthly mean LeW and those of a proxy for Ku-band radar penetration depth. Following the approach of Michel et al. (2014), this proxy is defined as the difference (Δh) between elevations obtained from the ICESat-2 laser altimeter and the CryoSat-2 radar altimeter. It is computed as:

$$\Delta h = h_{\mathrm{ICE2}} - h_C - (h_{\mathrm{DEMI}} - h_{\mathrm{DEMC}}), \tag{3}$$

where h_{DEMI} and ~~Δh for all valid~~ h_{DEMC} represent the elevations of the 100 m resolution ArcticDEM at the ICESat-2 and CryoSat-2 measurement locations, respectively. The subtraction of their difference accounts for terrain-induced elevation variations between the two measurement locations.

All negative Δh ~~estimations throughout the entire studied period. Furthermore, to assess the reliability of~~ values are excluded from further analysis. As shown in Fig. 2, these values predominantly occur near the margins of the LRM zone, particularly around Jakobshavn Glacier. From the overall probability distribution function, also shown in Fig. 2, we conclude this affects 7% of all values. Negative Δh values can be explained in different ways. Among others as the result of measurement errors, errors in data processing (notably in the ~~derived correlation between parameters, a p-value representing the significance of the~~

correlation is computed for each correlation coefficient; the correlation coefficient is insignificant when the p-value exceeds 0.05 (Bermudez-Edo et al., 2018).

3.4 Interpretation of LeW's spatio-temporal variation

Following the previous analysis, we adopt the 50 km×50 km grid over Greenland to obtain sufficient monthly LeW data (as mentioned in Section 2.2) between 2011 and 2021. After the monthly gridded LeWs are obtained, we compute the average LeW between January and May every year, and assess corrections for slope-induced errors), potential scattering errors from ICESat-2 measurements (Smith et al., 2018; Fair et al., 2024) and the difference in the averaged LeW between (i) every year and its previous year, and (ii)every year and 2011, respectively. With the first comparison, we asses the annual changes in volume scattering as melt events typically occur within summer season (June to August) (Tedesco and Fettweis, 2020). With the second comparison, we assess the LeW recovery since the extreme 2012 melt event (Tedesco et al., 2013)resolution between laser and radar altimetry (ICESat-2 might resolve topographic variability that cannot be resolved from radar altimeter data).

To assess the correlation between LeW variations and Δh, we first obtain all the Δh and LeW over the entire period within each grid cell of a 10 km×10 km grid. Correlations are quantified using the Pearson correlation coefficient. Statistical significance is evaluated via p-values, with correlations considered significant when $p \leq 0.05$ (Bermudez-Edo et al., 2018).

To analyse the LeW variation with respect to the

3.4 Comparison with modelled firn properties

The comparison with modelled firn properties , we perform the same two-fold time series analysis as proposed in Section ??, where the spatio-temporal variations of LeW , FAC, MAR densities and IMAU-FDM densities are juxtaposed and compared. The comparison is performed aims to examine (i) the capability of LeW to indicate firn processes and (ii) whether these processes are recent, providing insights for future studies. In doing so, we compare LeW variations against variations in modelled firn properties over two different time periods. The first one is between 2011 and 2021, when the comparison is conducted over the period for which CryoSat-2 Baseline D E data are available . This comparison is purely to assess the capability of LeW to indicate firn processes. (between 2010 and 2024). The second comparison is performed between 1960 and 2020, covers the longer period when IMAU-FDM data are available . (between 1960 and 2020). To ensure consistency with the LeW variability in Sect. 3.1, for the former analysis (using data between 2010 and 2024), we present the monthly mean density and FAC time series relative to the mean density and FAC from October 2010 to April 2011. This comparison is a supportive assessment to understand whether the firn processes are recent, and to provide insight and indications for future studies. also performed over the north–south transect and across ten elevation bands, introduced in Sect. 3.1. For the analysis over the longer period, we present the yearly mean density and FAC relative to the density and FAC from 2011.

In addition, for the analysis where we compare and interpret the spatio-temporal variations with firn properties, we need to select a maximal proxy for penetration depth that corresponds to the vertical resolution of the available firn models (i.e., MAR and IMAU-FDM) to ensure a fair comparison. Figure 2 shows that Δh is generally between 0 and 1.5 m on the interior of the ice sheet, therefore this range is used to select the max Δh that can be used as an indicator of volume scattering. Due to the

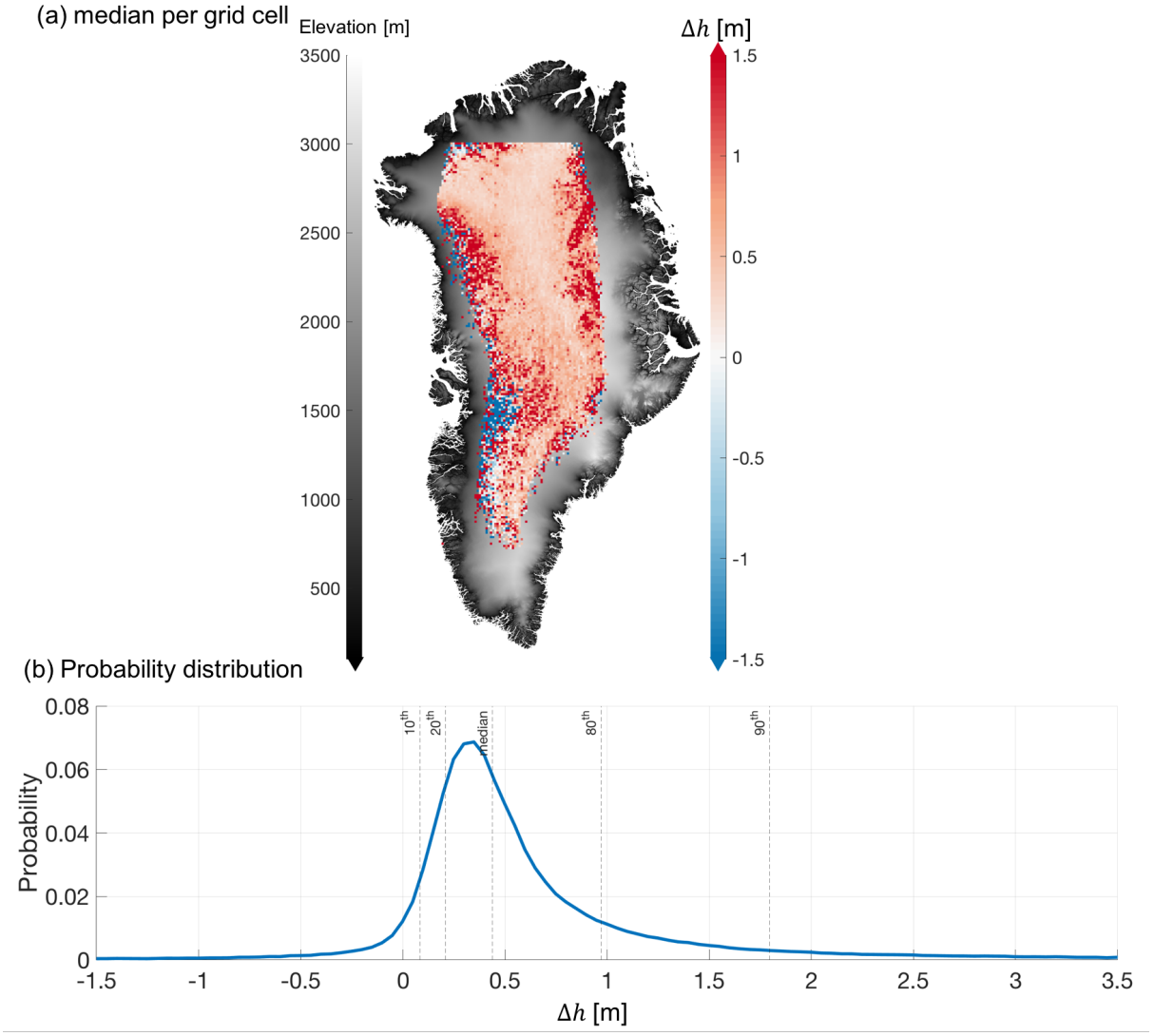

Figure 2. Statistics of elevation differences between ICESat-2 and CryoSat-2 (Δh). (a) Median Δh per grid cell at a 10 km×10 km grid; the background shows the 1 km ×1 km ArcticDEM. (b) Probability distribution function of Δh, with vertical lines indicating selected percentiles.

uneven vertical resolution of MAR, the weighted average density of the upper 1.5 m is calculated using the thickness per layer as the weighting factor.

4 Results

4.1 LeW ~~time series compared with vertical stratigraphy~~variability and recovery after the 2012 melt event

~~Figure ?? presents the time series of vertical stratigraphy dz, alongside the time series of LeW. Both dz and LeW are generally high near the western margins, reaching up to around~~

Figure 3a presents the changes in non-melt season (October–April) average LeWs between successive seasons. It shows a notable reduction (greater than 2 m~~and 25 m, respectively. In contrast, both values are low in the high-elevation~~) in LeW over the interior of the ice sheet ~~, with dz ranging from −0.2m to 0.1m and LeW between 5 m and 8~~between the non-melt seasons of 2011 and 2012, followed by increases between 2013 and 2015, with an increase of approximately 0.5 m. ~~However, in the southwest ablation zone, a low dz of around 0.1 mis observed , while LeW remains high at approximately 25 m.~~

~~dz is approximately 0.5 m higher in~~ This initial reduction indicates a decrease in volume scattering, corresponding to the extreme melt event and subsequent ice-lens formation in 2012 (Tedesco et al., 2013; Nilsson et al., 2015). The recovery between 2013 ~~than in the earlier years, but decreases to lower values between 2014~~ and ~~2019. In contrast, the reduction in LeW persists over a longer period. During the period from 2013 to 2019, LeW values from CryoSat-2 are 2 m to 3 m lower compared to the period between 2011 and 2012.~~ 2015 suggests a return to stronger volume scattering, likely due to new snow deposition hence the downward movement of ice lenses (Rennermalm et al., 2021).

~~Increases in dz are linked to the formation of ice slabs (Rutishauser et al., 2024). The recovery of dz after 2013 suggests that the deposition of new snow between 2014 and~~ Similarly, between 2018 and 2019~~covered the ice slabs beyond the MCoRDS' penetration depth.However, our LeW time series indicates that this recovery is not reflected in~~ , LeW experiences another minor drop of about 1 m, which coincides with the early melt observed in April and May 2019 (Tedesco and Fettweis, 2020) and the strong melt events between June and December 2018 that reduced volume scattering. Between 2019 and 2023, LeW increases and decreases alternately occur over the northern and southern parts of the interior of Greenland.

Figure 3b compares the non-melt season average LeWs of each year with the 2010 non-melt season average, highlighting long-term variations relative to the extreme melt year of 2012. All years show a negative difference in the interior to western side of the ice sheet, except for the difference between 2010 and 2011, indicating that after the 2012 melt, LeW does not fully recover. It remains approximately 1.5 m below 2010 levels in the centre-west of the ice sheet. The area with negative values (i.e. no LeW recovery since 2012) shrinks between 2013 and 2018, expands again in 2019, remains stable until 2021, and recovers again until 2023.

When combining Figs. 3a and b, a notable recovery in LeW since 2012 is evident. Our interpretation of the LeW patterns suggests that in the region that shows this reduction–recovery pattern, the snow was initially dry before the 2012 melt, resulting in LeW patterns dominated by large volume scattering. The 2012 melt and the subsequent refreezing reduced volume scattering, ~~as LeWcontinues to show reduced scattering due to subsurface high-density layers. This reduced volume scatteringis consistent~~

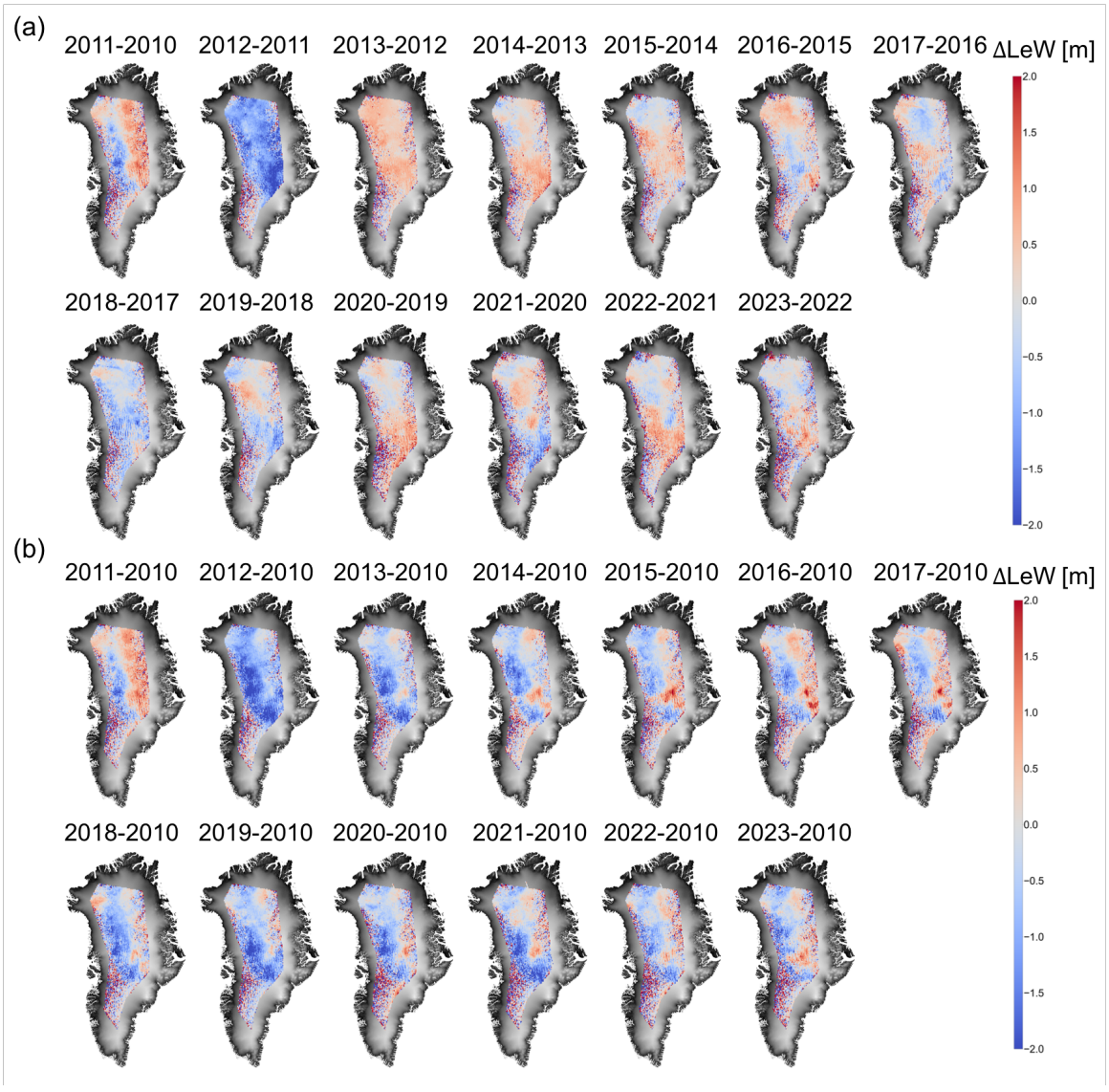

Figure 3. ~~Upper: *dz* computed by Rutishauser et al. (2024); lower: LeW~~ (a) Changes in non-melt season (October–April) average LeWs between successive seasons, and (b) changes in non-melt season average LeWs for the ~~corresponding time of acquisition as *dz*~~seasons 2011–2023 relative to the 2010 non-melt season average. ~~The background is~~ Years refer to the ~~1 km × 1 km DEM from Helm et al. (2014a, b) focusing on Greenland~~start of each non-melt season.

~~with the elevated firn densities shown in Figure~~causing a drop in LeW. LeW gradually recovered as the refrozen layer was buried, leading to the restoration of volume scattering. However, this recovery can be interrupted by more recent and frequent melt events, depending on the specific region. This interpretation can be supported by in situ measurements shown in Fig. 1. ~~At locations such as N2E06, EGRIP and T12, thin (approximately 0.1 m)~~ In most of the in situ firn profiles acquired after 2012, an elevated firn density (≥ 500 kg m^{-3}) can be observed between 0.4 m and 5 m depth, depending on the time and location of the acquisitions. Typically, if the acquisition time of the in situ measurement is closer to the 2012 melt event (e.g. the Schaller et al. (2016a) acquisition), the high-density ~~(more than 500 $kg\ m^{-3}$) layers persist at around 1.5 m in 2015 or 2017.~~ layer is shallower.

4.2 ~~Assessment~~ Effects of ~~the contribution of~~ surface ~~scattering to~~ roughness (changes) on LeW ~~variations~~(changes)

The comparison of ~~the LeW and~~ LeW and wavelength-scale surface roughness time series between 2013 and 2019 ~~, shown in Figures 4a and c, reveals a clear~~ (Figs. 4e and g) reveal a clear spatial correspondence between these ~~two~~ variables. Zones of high ~~surface roughness (greater than 6×10^{-4}~~roughness ($> 6 \times 10^{-4}$ m) coincide with elevated LeW values (~~greater than 9~~> 5 m) around pixels C and D. The region south of pixel C corresponds to Fig. 4 of van den Broeke et al. (2023), where the modelled melt extent exceeds ~~10 $kg\ m^{-2}\ yr^{-1}$~~10 kg m^{-2} yr^{-1}. Similarly, in ~~Figures 4b and d~~Figs. 4f and h, regions with high LeW (~~greater than 14~~> 7 m) are associated with increased wavelength-scale surface roughness (~~greater than 8×10^{-4}~~$> 8 \times 10^{-4}$ m) at elevations below 1800 m.

We also compare the spatial LeW variations with macro-scale roughness where the wavelength-scale surface roughness data are not available. Figure 4~~e demonstrates that the spatial variation in topography~~ i shows that macro-scale surface roughness follows a similar pattern to ~~the~~ LeW (Fig. 4~~a~~e), with a high standard deviation of elevation per grid cell (~~greater than 50~~> 50 m) around pixel D~~, where the roughness data is not available. Figure 4f shows that the complexity of the topography~~ . Fig. 4j illustrates that the macro-scale surface roughness decreases with increasing elevation, ~~a trend that mirrors~~ mirroring the LeW pattern in ~~Figure 4b~~Fig. 4f, where LeW generally increases as elevation decreases.

~~This~~ The aforementioned combined analysis of ~~surface roughness and topography indicates that~~wavelength-scale and macro-scale surface roughness indicates that, spatially, LeW tends to ~~increase in areas where surface roughness is high and the topography is complex.~~ be higher in areas with increased roughness. Figures 4a–d investigate how the melt–refreeze events and the subsequent snow deposition affect the temporal variations in LeW and wavelength-scale surface roughness (the macro-scale roughness is temporally invariant in our study). Figures 4a and b show a generally increasing LeW following the 2012 melt event, both in regions north of pixel C and in elevation bands higher than 2000 m. On the contrary, the wavelength-scale surface roughness varies rather arbitrarily. Among all the investigated pixels along the north–south transect, the temporal correlation coefficients between LeW anomalies and wavelength-scale surface roughness anomalies vary between -0.67 and 0.46. Among the ten elevation bands, the correlation coefficients vary between -0.12 and 0.26. Both sets of the correlation coefficients indicate low temporal correspondence. This comparison shows that the snow deposition following the melt–refreeze events mainly effects the LeW by affecting volume scattering, while the surface scattering temporal variations play a minimal role in LeW temporal variations.

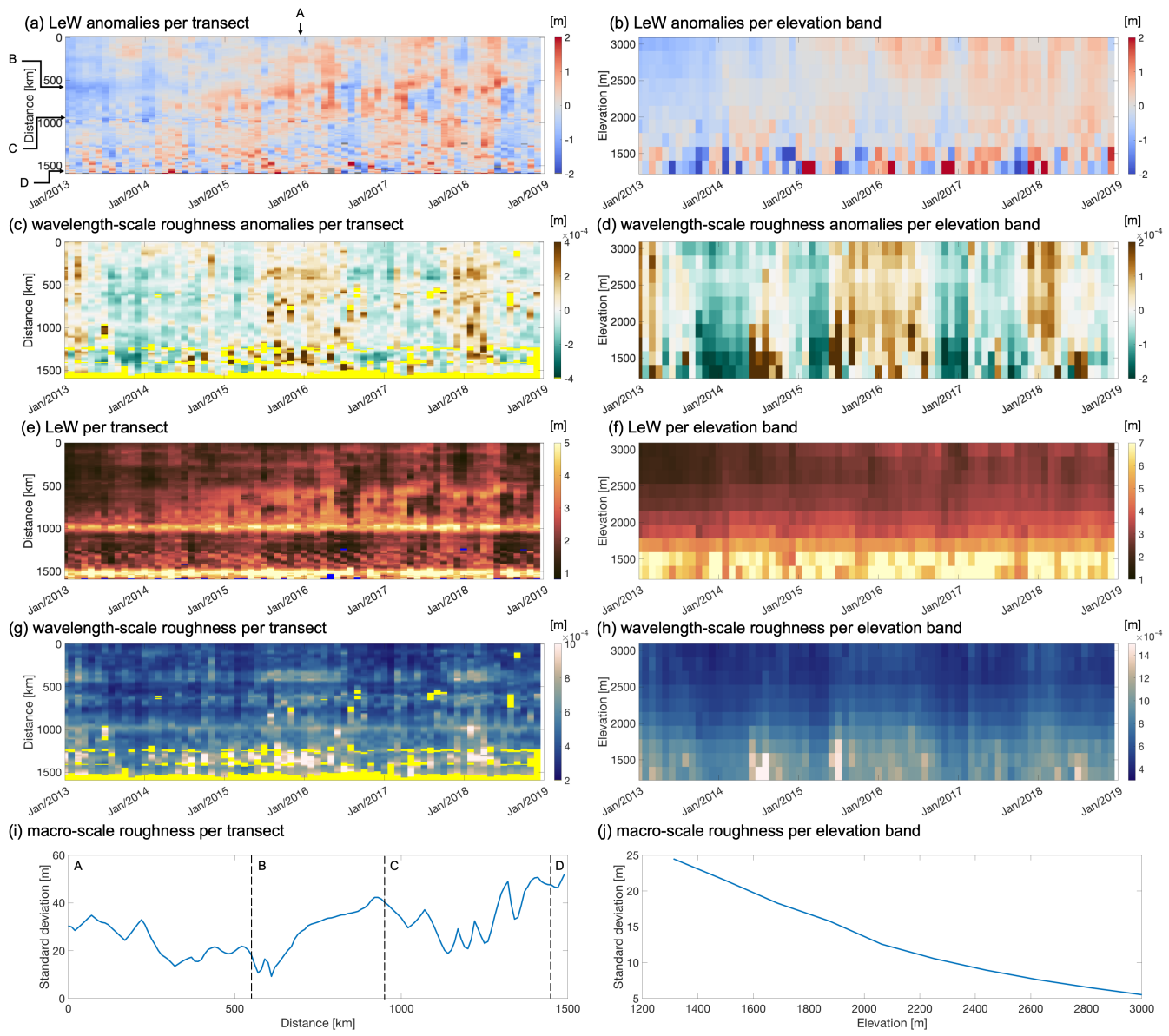

Figure 4. (a),(c),(e),(g),(i) LeW anomalies, wavelength-scale surface roughness anomalies, LeW, wavelength-scale surface roughness (represented by surface root mean square ~~(RMS)~~ height in unit of metres), and ~~variability of the topography~~ macro-scale roughness (represented by the standard deviation of ArcticDEM per ~~50~~10 km ~~pixel~~cell) along the north–south transect, respectively. A–D correspond to the inspected ~~pixels~~ grid cells highlighted in Fig. 1. (b),(d),(f),(h),(j) LeW anomalies, wavelength-scale surface roughness anomalies, LeW, wavelength-scale surface roughness, and ~~topography~~ macro-scale roughness grouped by the ~~10~~ ten elevation bands, respectively. ~~Orange~~ Grey colour ~~indicates~~ in (a), blue colour in (e), and yellow colour in (c) and (g) indicate that the data are not available.

4.3 ~~Assessment of correlation~~ Correlation between LeW and ~~Δh~~laser-radar height offsets

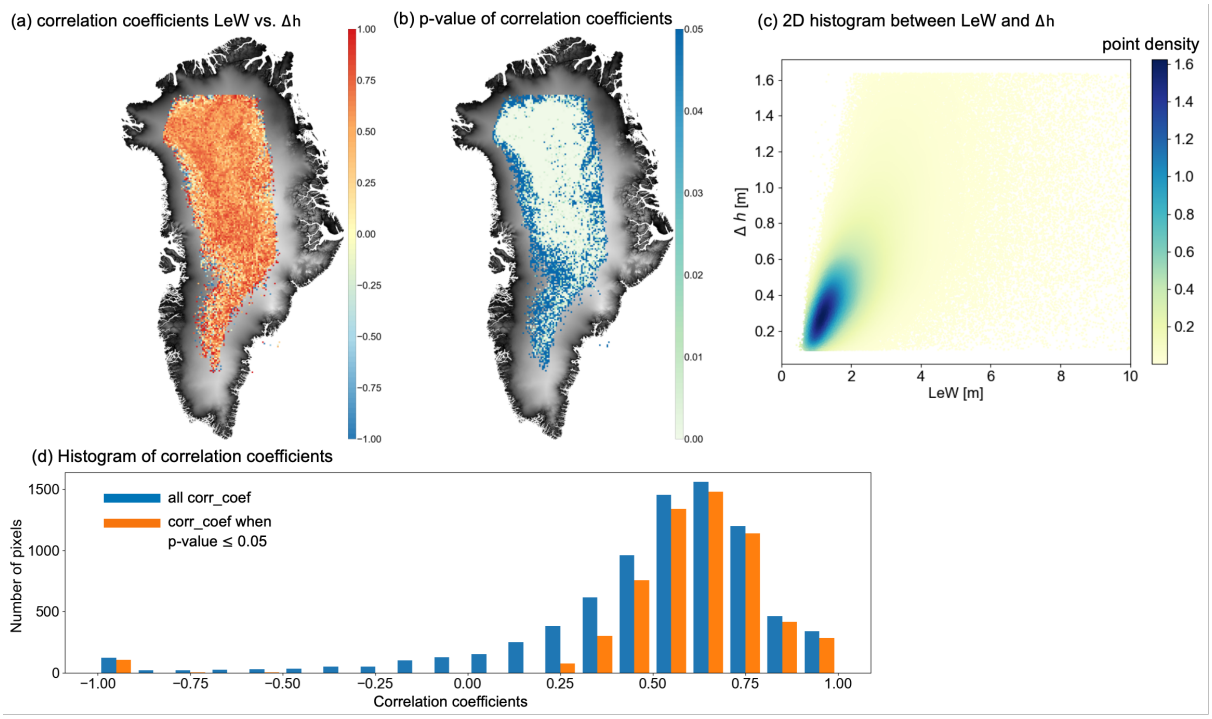

Figure 5. (a) Map of correlation coefficients between ~~Δh and~~ LeW ~~,~~ and Δh. (b) Corresponding map of p-values ~~of~~ for the correlation coefficients between ~~Δh and~~ LeW and Δh. The background is the 1 km $\times$1 km ~~DEM from Helm et al. (2014a, b) focusing on Greenland~~ArcticDEM. (c) ~~Histogram~~ 2D histogram showing the relationship between all LeW and Δh data points, with point density estimated using a Gaussian kernel (Węglarczyk, 2018). (d) Histograms of ~~correlation coefficients when~~ all correlation coefficients ~~are considered in~~ (blue~~,~~) and ~~when only~~ statistically significant correlation coefficients ~~are considered~~ (~~p-value≤ 0.05) in~~ $p \leq 0.05$, orange).

Figure 5 presents the correlation coefficients between the LeW and Δh ~~and LeW~~ time series for each ~~25 km$\times$25~~10 km$\times$10 km grid cell. ~~Overall, within~~ Across the CryoSat-2 LRM ~~coverage, LeW and Δh exhibit a generally~~ zone, the two parameters generally exhibit a positive correlation, with a median value of approximately ~~0.3. The histogram in Figure 5c further highlights that the correlation between LeW and Δh tends to be positive over the study areas.~~

~~The significance of these correlations, as indicated by the p-values, shows that the correlation coefficients are generally more significant in the interior of the ice sheet compared to the margins. When applying a threshold (0.05)on the p-value to focus on pixels with high significance, the~~ 0.6. Fig. 5b shows, however, that most correlation coefficients at the margin of the LRM zone are not significant ($p > 0.05$). Excluding them has minimal effect on the median correlation coefficient~~increases to 0.4~~; it remains around 0.6. The lower correlation and significance towards the margins can likely be attributed to ~~higher surface scattering, which is caused by surface roughness and topographic variation (Legrésy and Rémy, 1997; Nilsson et al., 2015), as demonstrated earlier in Section 4.2.~~ the compromised performance of ICESat-2 elevation measurements due to the large slopes,

rough surfaces (Smith et al., 2023c) and scattering biases in the low-elevation regions (Smith et al., 2018). These biases can be propagated to the derived Δh, which may not properly indicate volume scattering variations.

The positive correlation ~~between LeW and Δh~~ suggests that as LeW increases, the ~~penetration depth of CryoSat-2~~ laser-radar height offset also increases, indicating a rise in volume scattering. However, the correlation coefficients ~~remain below 0.5~~ do not exceed 0.9 overall. This aligns with the findings of Nilsson et al. (2015), which showed that LeW was more sensitive to ice-lens formation and volume scattering variations than Δh. ~~Nevertheless~~Therefore, LeW was used as an indirect parameter to assess volume scattering, particularly when ICESat-2 data were not available.

4.4 ~~Assessment of inter-annual~~ LeW variations versus model-derived firn property variations

~~(a) Difference between the average LeW between January and May of every year and the average LeW between January and May of the previous year, and (b) difference between the average LeW between January and May of every year and the average LeW between January and May of 2011. Pixels A–D are labelled in the upper-left panel of (a).~~

~~Figure 3a presents the differences in averaged winter–spring LeW between consecutive years. It shows a significant reduction (greater than 2 m) in LeW over the interior of the ice sheet between 2012 and 2013, followed by a recovery between 2013 and 2015, with an increase of approximately 0.5 m. This initial reduction in 2012—2013 indicates a decrease in volume scattering, corresponding to the extreme melt event and subsequent ice-lens formation in 2012 (Tedesco et al., 2013; Nilsson et al., 2015). The recovery between 2013 and 2015 suggests a return to stronger volume scattering, likely due to new snow deposition hence the downward movement of ice lenses (Rennermalm et al., 2021).~~

~~Similarly, between 2018 and 2019, LeW experiences another minor drop of about 1 m, which coincides with the early melt observed in April and May 2019 (Tedesco and Fettweis, 2020) and the strong melt events between June and December 2018 that reduced volume scattering. Between 2019 and 2020, LeW increases are observed in the northern part of the ice sheet, while decreases are noted in the southeast.~~

~~Figure 3b compares the average LeW (from January to May) of each year with the average LeW of 2011, highlighting long-term variations relative to the extreme melt year of 2012. All years show a negative difference in the interior of the ice sheet, except for the difference between 2011 and 2012, indicating that after the 2012 melt, LeW does not fully recover. It remains approximately 2 m below 2011 levels in the centre of the ice sheet. The area with negative values (i.e., no LeW recovery since 2012) shrinks between 2013 and 2018, expands again in 2019, and remains stable between 2019 and 2021.~~

~~When combining Figs. 3a and b, a notable recovery in LeW since 2012 is evident. This recovery can be attributed to new snow deposition on top of the ice lenses, although it was interrupted by the melt event in 2019.~~

4.5 ~~Assessment of LeW time series in relation to firn property variations~~

Figure ~~A1 shows the~~ 6 shows the anomalies in monthly mean LeW, MAR density, IMAU-FDM density, and ~~normalised~~ FAC time series along the transect highlighted in Fig. 1 ~~. The most significant~~ (the absolute time series of these parameters are provided in Fig. A1). The most pronounced reduction in LeW (by 1–3 m compared to the non-melt season of 2010–2011) in Fig. ~~A1~~6a aligns with the sharp decrease in 2012, also shown in Fig. 3.

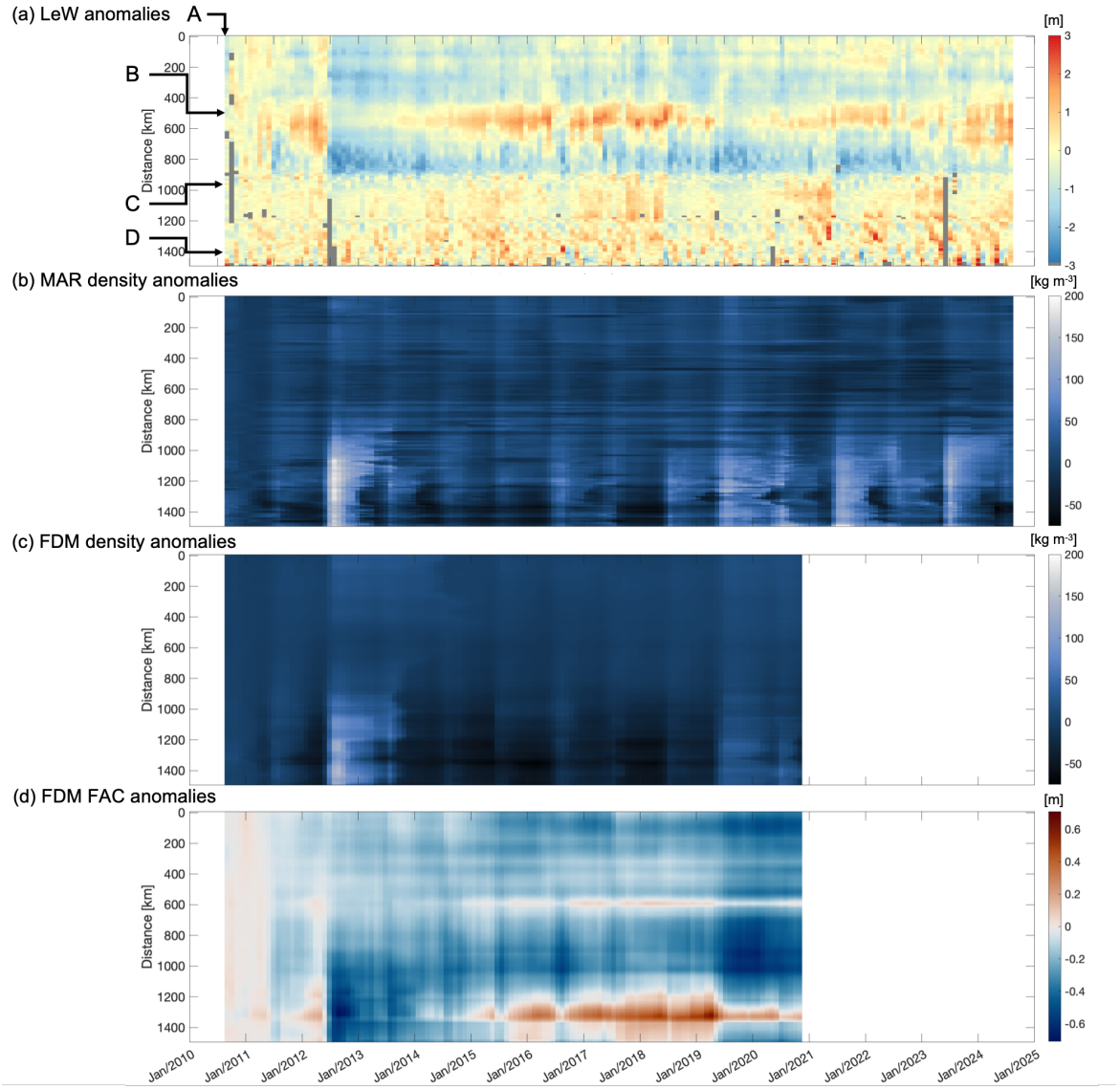

Figure 6. ~~Monthly~~ Anomalies (with respect to the mean between October 2010 and April 2011) in monthly mean LeW, ~~daily~~ MAR density of the ~~1~~st top 1.5 m of ~~snow~~firn, ~~10-day~~ IMAU-FDM density of the top 1.5 m of firn, and IMAU-FDM firn air content (FAC) time series per pixel along the transect visualised in Fig. 1. The FAC time series are normalised with respect to the long-term mean of each pixel. The y-axes refer to the distance from the northernmost pixel. Arrows indicate the inspected pixels A–D. ~~Large LeW decreases with respect to the previous month~~ Grey colour in (~~exceeding 0.5 m~~a) ~~for pixels north of pixel C are labelled. Orange (a–c) or grey (d) colour~~ indicates the values that are not available.

In the Along the investigated transect, in the pixels north of pixel C, the monthly mean LeW is generally high (above 8 m) before a clear recovery in LeW can be observed after the 2012 melt event, after which it abruptly drops below 6 m and gradually recovers until 2018. Along with the LeW reduction in 2012, both the MAR and IMAU-FDM models show increased average densities in the upper 1.5 m due to refreezing (Fig. A2c). Since 2018, LeW has fluctuated around 8 m, with annual drops occurring each summer from 2018 to 2021. Although these yearly declines are not as prolonged as in 2012, they occur more frequently than before 2018. Additionally, in . Between pixels B and C, the recovery is disrupted again in summer 2019, the normalised FAC in these regions drops by approximately 0.1 m and remains lower than pre-2019 levels. The density also increases, remaining higher than both (i) pre-2012 levels and (ii) levels between 2014 and 2019. These observations align with corresponding to another extensive melt event (Tedesco and Fettweis, 2020) and the observation in Fig. 3, which shows that LeW in the interior of the ice sheet dropped after the 2012 melt event, gradually recovered between 2014 and 2019, and stabilised between 2019 and 2021, remaining about 2 m below 2011 levels.

In the pixels south of pixel C along the transect, the monthly mean LeW since 2011 2010 does not show significant anomalies notable anomalies (e.g. reduction by 1–3 m compared to the non-melt season of 2010–2011, as observed for pixels north of pixel C) related to melt events (Fig. A2b). These pixels experience are characterised by recurrent melting each year , as indicated by the density time series, which increase every summer. Densities in the southern pixels are also 10 $kg\ m^{-3}$ to 60 $kg\ m^{-3}$ higher than those in the north, and the drop-and-recovery pattern of FAC is more pronounced in the south. Additionally, the regions around pixel C and pixel D exhibit consistently higher LeW values (greater than 12 m) than those between pixels C and D (6 m to 8 m). (Fig. A2b) and higher snow accumulation rate (Fig. A2d). However, moments of LeW reduction can be observed in summer 2018, 2019, 2021 and 2023, corresponding to the high meltwater production and refreezing (>5 mmWE per month) in Figs. A2b–c.

Our interpretation of the LeW patterns suggests that in the region between pixels A and C, the snow was initially dry before the 2012 melt, resulting in LeW patterns dominated by large volume scattering. The 2012 melt and the subsequent refreezing reduced volume scattering, causing a drop in LeW. LeW gradually recovered as the refrozen layer was buried, leading to the restoration of volume scattering. However, this recovery was interrupted by more recent and frequent melt events. In contrast, the regions south of pixel C show relatively stable LeW throughout the time series, as the melt–refreeze cycle occurs annually, causing less dramatic changes in volume scattering. Finally, the high LeW around pixels C and D is likely due to increased surface scattering caused by surface roughness and topography (Legrésy and Rémy, 1997), as discussed earlier in Section 4.2.

Figure A3 shows the variations 7 shows the anomalies in LeW, MAR density, IMAU-FDM density, and IMAU-FDM FAC (normalised relative to the long-term mean) between January 2011 and August 2021 between September 2010 and September 2024 for different elevation groups.bands (the absolute time series are shown in Fig. A3). In the low-elevation regions (below 18001600 m), the LeW remains consistently high (around 20 m), with seasonal fluctuations of approximately 2 m during several years. For example, LeW decreases by about 2 m between June and August in 2013, 2014, 2015, 2018, and 2019. The density in variation does not show a regular temporal pattern. On the contrary, these low-elevation areas also remains higher than in other parts of Greenland, with noticeable seasonal variations (densities increase demonstrate more notable seasonal variations in density and FAC (large density increases and FAC decreases in June) compared to other elevation bands. These

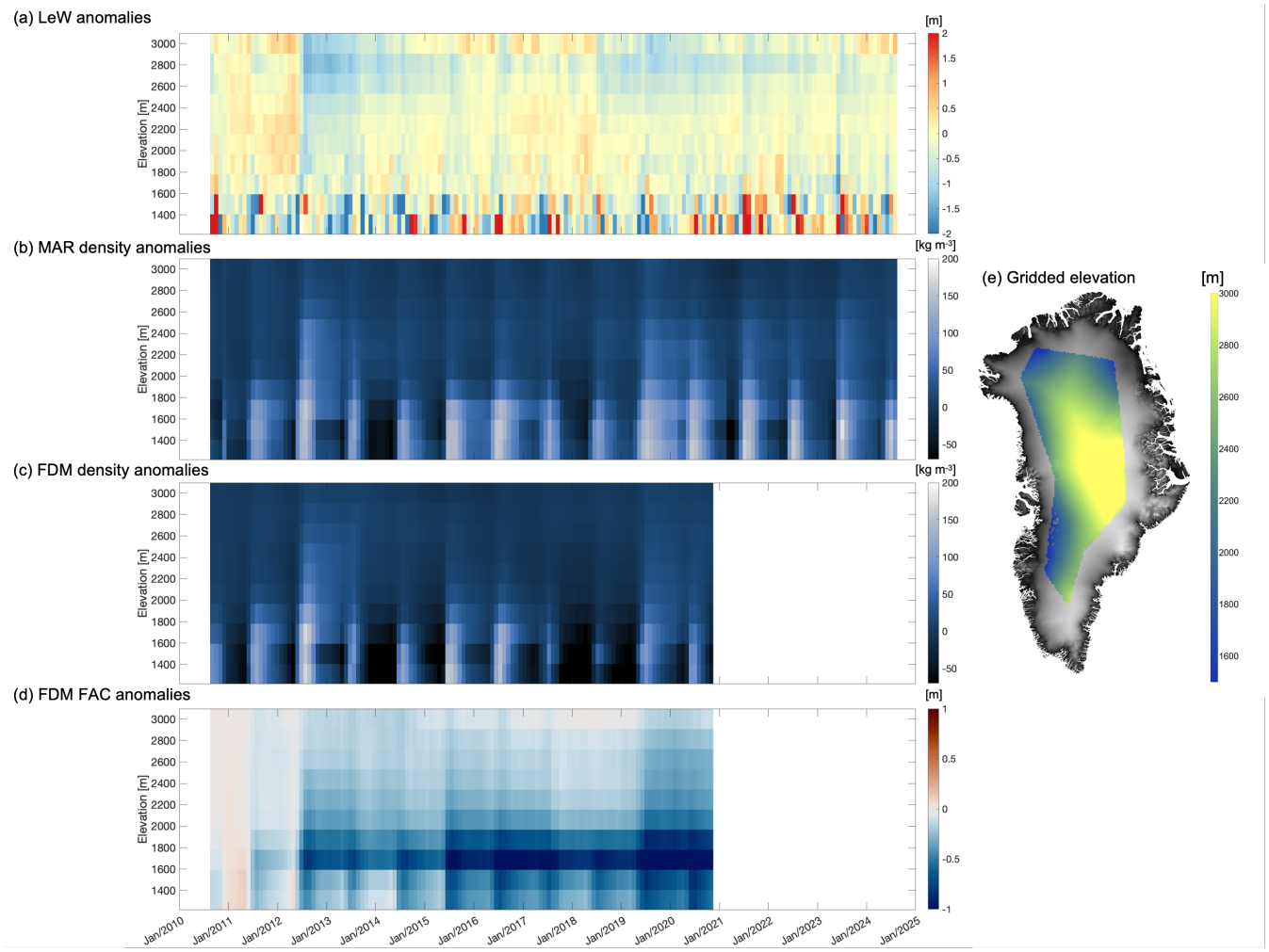

Figure 7. ~~Time~~ Anomalies (with respect to the mean between October 2010 and April 2011) in time series of monthly mean LeW, ~~daily~~ density from MAR, ~~10-day resolution~~ density from IMAU-FDM, and ~~normalised~~ FAC from IMAU-FDM, grouped by a down-sampled (gridded) DEM. ~~Orange (a–c) or grey (d) colour indicates that the data are not available.~~ A map of the gridded DEM is provided on the right (e), with the original 1 km ×1 km ~~Helm et al. (2014b) DEM~~ ArcticDEM as background.

density increases ~~coincide with annual decreases in normalised FAC between June and August which correspond to the melt season.~~ and FAC decreases coincide with the annual melt season (Fig. A4b–c).

Above the ~~1800~~1600 m elevation, a reduction in LeW is observed across all elevation ~~groups~~ bands following the 2012 melt event. The largest reduction is approximately 2 m~~in the 1800 m–2200 m elevation range, and approximately 5 m~~, occurring in regions above ~~2200~~2500 m. This LeW reduction in mid-2012 corresponds to the ~~widespread~~ extensive melting, increased densities in both MAR and IMAU-FDM models, and a decline in ~~normalised~~ FAC. Smaller increases in density and decreases in FAC were also observed in mid-2015, mid-2016, and mid-2019 above 1800 m, with a slight decline in LeW during mid-2015, mid-2016, and mid-2018.

From the time series, we also observe that in the 1800 m–2200 m range, the LeW recovery rate is faster than in regions above 2200 m (approximately 0.6 ~~$m\ yr^{-1}$~~ m yr^{-1} versus 0.2 ~~$m\ yr^{-1}$~~ m yr^{-1}). By spring 2018, in areas above 1800 m, the LeW had nearly returned to pre-2012 levels (about 1 m lower). However, it temporarily dropped in mid-2018 by about ~~1.5~~0.5 m and ~~has since fluctuated around that level~~experienced another recovery process. This trend is consistent with the observations in Fig. 3b. Notably, our time series ~~indicates~~ indicate that aside from the well-documented 2019 melt event (Tedesco and Fettweis, 2020) (characterised by density increases and FAC decreases), a ~~change in volume scattering already occurred in mid-2018. This led to a~~ slight decrease in LeW above 2200 m has been observed in mid-2018, suggesting reduced volume scattering. However, unlike other events, the LeW decrease in mid-2018 does not correspond to a density increase or FAC decrease in the models. Finally, both MAR and IMAU-FDM densities demonstrate an annual cycle, while LeW does not show a pronounced annual pattern. This difference could be explained as follows. The annual density increase may not be caused by the melt and refrozen layers, therefore does not sufficiently cause a reduction in radar volume scattering hence a reduction in LeW. Therefore, LeW may only react to the strong melt–refreeze events.

Finally, Fig. 8 displays the anomalies in monthly mean LeW between 2010 and 2024, and the annually mean IMAU-FDM density and ~~normalised~~ FAC time series from 1961 to 2020 for different elevation ~~groups, alongside CryoSat-2 LeW data from the past decade~~bands. This comparison aims to determine whether the changes in volume scattering observed in CryoSat-2 LeW show a recent instability in Greenland's firn. ~~Below 2800 m, densities have increased by 5 $kg\ m^{-3}$ to 20 $kg\ m^{-3}$ since 2012, while regions above 2800 m show only a slight increase (by about 3 $kg\ m^{-3}$) over the same period. In the pastdecade, FAC below 2200~~In the past decade, the firn density of the upper 1.5 m is notably higher (up to 50 kg m^{-3}) than that in the past. FAC below 2000 m dropped ~~significantly~~ considerably compared to earlier periods.~~In contrast, FAC values above 2200 min the past decade are similar to those observed between 1975 and 1985, although they are lower than FAC values between 1985 and 2010. Additionally, between 2011 and~~ In the elevation bands above 2000 m, between 2012 and 2020, FAC experienced ~~slight~~ drops and recoveries that correspond to the LeW pattern between 2012 and 2018, followed by another decline between 2018 and 2020, which also aligns with LeW trends. However, in these elevation bands, the FAC level overall remains at the same level as the FAC level before 1980. Therefore, we cannot yet conclude that the firn layer above 2000 m elevation has experienced fundamental altering in the past decade.

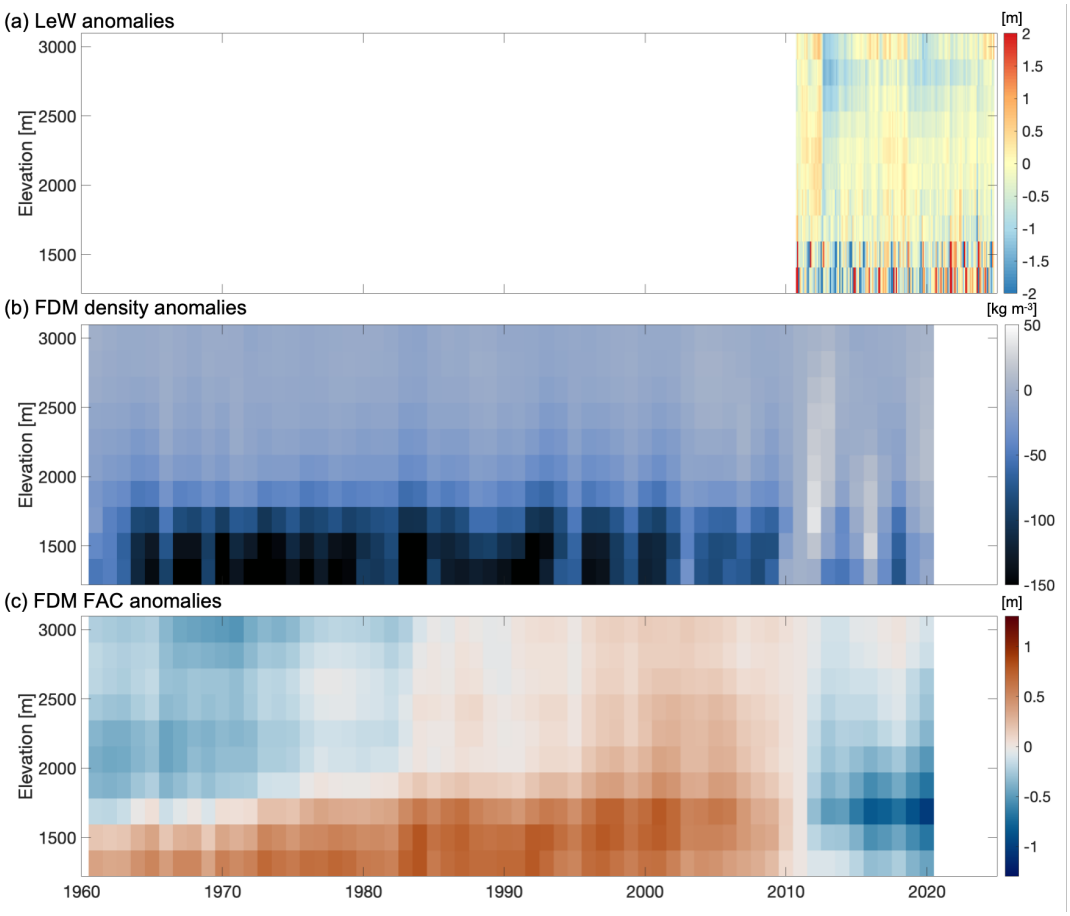

Figure 8. (a) ~~Annual~~ Anomalies (with respect to the mean ~~density~~ between ~~1961~~ October 2010 and ~~2020 from IMAU-FDM, grouped by gridded DEM.~~ April 2011) in time series of monthly mean LeW; (b)~~Density variation between 1961 and 2020 for selected gridded DEM groups; the annual mean densities are in solid lines and the 25–75th percentiles are shaded.~~ ,(c) ~~Annual~~ anomalies (with respect to the mean ~~FAC between 1961~~ of 2011) in time series of yearly mean density and ~~2020~~ FAC from IMAU-FDM, ~~normalised~~ grouped by ~~long-term mean of FAC for visualisation.~~ a down-sampled (~~d) Normalised FAC between 1961 and 2020 for selected~~ gridded~~DEM groups; the annual mean densities are in solid lines and the 25–75th percentiles are shaded. (e) CryoSat-2 LeW between 2011 and 2021 for selected gridded~~ DEM~~groups; the monthly mean densities are in solid lines and the 25–75th percentiles are shaded~~.

5 Discussion

This study explores the capability of using LeW derived from CryoSat-2 waveforms to assess the spatial and temporal variations of ~~the volume scattering properties of~~ firn in Greenland ~~. By comparing the LeW time series with the vertical stratigraphy from Rutishauser et al. (2024), we observed a slower recovery of firn following the 2012 melt event in the interior dry snow zone of Greenland compared to their findings. This discrepancy is likely due to LeW's focus on volume scattering, which contrasts with the limitations of dz in accounting for topography, roughness, and timing corrections of the MCoRDS signal, as noted by Rutishauser et al. (2024). Our findings suggest that CryoSat-2 LeW, with its greater sensitivity to volume scattering, provides a more reliable tool for assessing firn recovery in the dry snowzone, where surface scattering is minimal. Furthermore, the spatial and temporal continuity offered by CryoSat-2 is a significant advantage over Operation IceBridge (OIB) data, which is more spatially limited. CryoSat-2's Greenland-wide coverage enables a more comprehensive tracking of firn evolution, particularly in remote regions where OIB data may not be available, providing a more detailed overview of post-melt firn processes.~~caused by melt–refreeze events. By first showing the yearly revolution of LeW, we demonstrate that LeW can successfully capture the strong melt events such as in 2012, 2019 and 2021. It also demonstrates the recovery of the firn layer due to the deposition of new snow, which is consistent with the observation and prediction from Nilsson et al. (2015).

~~However, outside~~ Outside of the central dry snow zones, LeW is ~~less effective in tracking melt–refreeze processes~~constantly high, as surface features such as roughness and topography begin to dominate its ~~variability~~spatial variability (also noted by Ronan et al. (2024)). This was confirmed through comparisons with ArcticDEM, firn models, and the data from Scanlan et al. (2023)~~. To further validate~~ , where a high LeW spatially corresponds to a high wavelength-scale and macro-scale surface roughness. To distinguish whether the temporal variations in LeW are also caused by surface roughness, we derived the temporal anomalies in LeW and wavelength-scale surface roughness with respect to their mean between 2013 and 2018 (due to the limitation in data availability). This experiment shows that contrary to the spatial variations, the temporal variations in LeW are independent of variations in surface roughness. It is important to note that this experiment has not yet considered the temporal variability of macro-scale roughness, as it is derived from the static ArcticDEM data. Future studies are encouraged to investigate this by computing the standard deviation of elevations within different CryoSat-2 footprint at different acquisition time.

To further investigate LeW as a measure of firn volume changes, we compared it with ~~CryoSat-2 penetration depth~~ laser-radar height offsets (calculated as the height difference between ICESat-2 and CryoSat-2). Overall, the relationship is similar to the conclusion of Michel et al. (2014), who proposed a linear function between LeW and penetration depth in flat regions of Antarctica. Our study, although not explicitly defining a "flat" region, delineated the interior of Greenland where the correlation between LeW and ~~penetration depth~~ laser-radar height offsets is positive (around ~~0.3~~0.6) and is significant ($p \leq 0.05$). ~~By distinguishing areas where LeW is dominated by volume scattering from those dominated by surface scattering~~In this region, it is most probable that the temporal LeW variations can be caused by variations in volume scattering. Therefore, our study provides a valuable framework for understanding firn response to melt events across different regions of Greenland.

This study is the first known demonstration of a Greenland-wide (within the CryoSat-2 LRM data coverage) LeW time series analysis, supported by two different firn models. The time series between ~~2011 and 2021~~ 2010 and 2024 show that the 2012 melt event had a more prolonged impact than any other following melt events, resulting in a reduction in LeW that persisted until 2018, especially over the central-west Greenland. Recurrent melt events since 2018 have interrupted the firn recovery that was expected by Nilsson et al. (2015), underscoring the importance of monitoring these processes over long timescales. These findings highlight the value of CryoSat-2 LeW in assessing post-melt firn evolution, particularly at higher elevations.

When observed over a longer time scale (between 1960 and 2020), firn models indicate that the most pronounced firn changes, such as increases in density and decreases in FAC, occur below ~~1800~~1600 m elevation. At these lower elevations, LeW changes are less pronounced, ~~showing only a 2 m reduction.~~ not showing any clear temporal pattern compared to the mean LeW over the non-melt seasons between 2010 and 2011. In contrast, at elevations above ~~2250~~2000 m, LeW is comparably sensitive to the long-term effect of refreezing layer as FAC and density, while exhibiting higher sensitivity in 2018. This sensitivity suggests that LeW data could play a crucial role in refining firn models, especially for higher elevations, where existing models may underestimate the impacts of melt events on volume scattering.

Our findings indicate that in southern and low-elevation regions of Greenland, where surface scattering dominates and melt events are more frequent, LeW is less effective in capturing firn changes. Future studies could address these limitations by incorporating additional altimeter-derived parameters such as trailing edge slope (TeS), waveform peakiness, and backscatter coefficients, which are more sensitive to surface scattering processes (Nilsson et al., 2015). These parameters, combined with LeW, would offer a more complete picture of surface and volume scattering interactions.

To better simulate the complex contributions of surface and volume scattering, radiative transfer models (Adodo et al., 2018; Larue et al., 2021) can be employed. These models, when taking into account the varying viewing geometry of the satellite, can enable more accurate representations of how melt–refreeze processes (characterised by varying temperature, firn density, microstructure and grain size) impact firn properties.

The ongoing ICESat-2 mission should also continue to provide the opportunity to ~~derive~~ indicate Ku-band radar penetration ~~depth~~abilities, which also allows to continuously monitor changes in ~~sub-surface~~ subsurface firn due to melt–refreeze processes. This could complement CryoSat-2 data, offering a higher-resolution view of firn structure over time. ~~Additionally, combining~~ Combining radar altimeter data from different frequencies can also help derive volume scattering information from different subsurface layers~~, as suggested by Adodo et al. (2018), Otosaka et al. (2020),~~. According to Lacroix et al. (2008) who compared waveform parameters from S-band and ~~Scanlan et al. (2023). This~~ Ku-band radar altimeters, the impact of surface scattering as well as from snow grain size decreases with an increasing radar frequency. According to Scanlan et al. (2023) who derived firn properties using both Ku-band and Ka-band radar altimeters, radar altimeters operating in a lower frequency are sensitive to firn densities at a larger depth. For future dual-frequency radar altimeters, e.g. the Copernicus Polar Ice and Snow Topography Altimeter (CRISTAL) mission which operates in both Ku- and Ka-bands (Kern et al., 2020), the different penetration abilities and sensitivities to firn properties offer the potential of a multi-layered analysis approach. For a higher frequency such as Ka-band, the penetration depth is smaller, hence we expect a quicker recovery of LeW after a melt event than that of Ku-band. This different recovery rate can help future studies to locate the subsurface refrozen layers and derive

accumulation rate. Such a multi-layered approach can be particularly useful in regions where surface and volume scattering overlap, offering more nuanced insights into firn changes.

To enhance future firn studies, LeW data can be integrated into firn models to improve predictions of melt impacts on volume scattering, particularly at higher elevations. Although not presented in this study, the up-to-date Goddard Space Flight Center (GSFC) firn model (Medley et al., 2022) and Glacier Energy and Mass Balance (GEMB) firn model (Gardner et al., 2023) can also be incorporated in the satellite time series analysis by both qualitatively indicating the presence of subsurface ice lenses and by quantitatively deriving firn properties with radiative transfer models. By using interdisciplinary approaches, we can deepen our understanding of how melt events affect firn properties over the long term, improving our ability to predict future ice sheet dynamics.

6 Conclusions

This study explored and demonstrated the possibility for using the LeW derived by CryoSat-2 to assess spatio-temporal changes in Greenland firn status caused by ~~melt–refreezing~~ melt–refreeze events. While previous studies indicated a recovery pattern in LeW when new snow is deposited on top of the refrozen layers, our study further investigated whether this process can be observed with the help of LeW time series. Our analysis showed that the recovery speed can be related to the elevation and new snow deposition. However, the recovery is hampered by more recent melt events (although not as severe as the 2012 event). In central-west Greenland, the LeW never recovered to the pre-2012 level; in regions where LeW managed to recover, new melt events resulted in new LeW reductions, which indicates a reduction in volume scattering hence a reduction in its capacity to store meltwater. Such alternation can also be confirmed using the long-term time series, which showed a decreasing LeW, an elevated density and a decreasing FAC in recent decades. ~~This correspondence between the reduction in volume scattering and the reduction in FAC confirms that the more frequent melt events reduce the capability of Greenland firn to retain meltwater, and in turn may result in an accelerated runoff from the ice sheet (Vandecrux et al., 2019).~~

Finally, this study has demonstrated the reliability and limitations for using LeW from radar altimeter to understand the melt–refreeze processes and the subsequent volume scattering variations ~~and associated firnprocesses~~in Greenland firn, paving the way for the study of ~~sub-surface~~ subsurface firn processes in a changing climate. The use of a combination of CryoSat-2 and ICESat-2 height measurements can also contribute to the study of Ku-band penetration ~~depth~~ ability hence volume scattering variations induced by melt–refreeze events.

Code and data availability. Software for the in-house processing of CryoSat-2 data from L1b to L2 is available on request from Cornelis Slobbe. The MAR datasets are available on request on http://ftp.climato.be/fettweis/MARv3.14/Greenland/. The IMAU-FDM datasets are available on request from Max Brils. ArcticDEM is provided by the Polar Geospatial Center under NSF-OPP awards 1043681, 1559691, and 1542736. The DEM of Greenland used for result visualisation is provided by Helm et al. (2014a, b) under license Creative Commons Attribution 3.0 Unported. The CryoSat-2 L1b and L2I data are provided online by ESA and the ICESat-2 L3A data are provided online by NSIDC (https://nsidc.org/data/atl06). The surface roughness data is available on https://doi.org/10.11583/DTU.21333291.v1.

Appendix A: LeW and MAR melt, refreeze and total snow height time series

Figure A1 shows the absolute time series of LeW, MAR density and IMAU-FDM density, and the normalised IMAU-FDM FAC with respect to the long-term mean, along the north–south transect shown in Fig. 1. Over Greenland, FAC increases with elevation and exhibits substantial spatial variability, ranging from approximately 0 m at the ice sheet margins to over 20 m in the interior. However, when juxtaposing FAC over the entire study area, spatial variations are pronounced, whereas temporal variations are more subtle. To enhance the temporal signal relative to spatial variation, we subtract the long-term mean of each pixel (using the same grids as the resampled CryoSat-2 LeW) from the time series. Finally, monthly mean density and FAC are computed to align with the CryoSat-2 time series.

Figure A2 illustrates the time series of monthly mean LeW, MAR meltwater production, meltwater refreezing and accumulated total snow height change along the transect highlighted in Fig. 1. The meltwater production and refreezing correspond to the density increases in Fig. A1b. Figure A2a indicates that the overall decrease in LeW in 2012 corresponds to both the extensive meltwater production as well as refreezing. ~~Furthermore, a~~ A slight LeW decrease in mid-2019 between pixels A and C also corresponds with the ~~melt–refreezing~~ melt–refreeze event. By comparing Fig. A2a and Fig. A2d, we notice that ~~north of pixel B shows~~ pixels between pixels A and B show a slower LeW recovery than between pixels B and C, which corresponds to a lower cumulative total snow height change (i.e ~~snowfall accumulation) from the 12th of~~ snow accumulation) since the melt event in July 2012. However, around pixel B, the LeW recovery between 2014 and 2018 is higher that that between pixels A and B, despite a lower snow accumulation. This may be attributed by the difference in properties and structures of the upper firn layer (Ronan et al., 2024).

Figure A3 shows the absolute time series of LeW, MAR density and IMAU-FDM density, and the normalised IMAU-FDM FAC with respect to the long-term mean, grouped by the ten elevation bands. Similarly, we present the time series per elevation ~~group~~ band in Fig. A4. The melt–refreeze patterns correspond with the density increases in Fig. A3b. However, differently from Fig. A2a and Fig. A2d, Fig. A4a and Fig. A4d do not show a high correspondence between LeW recovery and total accumulated snow: the total accumulated snow height from ~~12~~ July 2012 shows the highest increase between 2014 and ~~2021~~ 2024 at around 2400 m elevation, while the fastest LeW recovery occurs between 1800 m and 2200 m. This discrepancy could be attributed to the significantly larger snow accumulation in the South of Greenland than the North, despite being at the same elevation.

Author contributions. WL, SL and BW designed the study. WL conducted data management, processing, and analysis; produced the figures; and provided the manuscript with contributions from the other co-authors. SL provided support on data visualisation and analysis. BW provided expertise for data analysis. CS provided expertise and software for radar altimetry processing and data analysis. XF generated the MAR outputs. MB generated the IMAU-FDM outputs.

Competing interests. Stef Lhermitte, Bert Wouters and Xavier Fettweis are members of the editorial board of The Cryosphere.

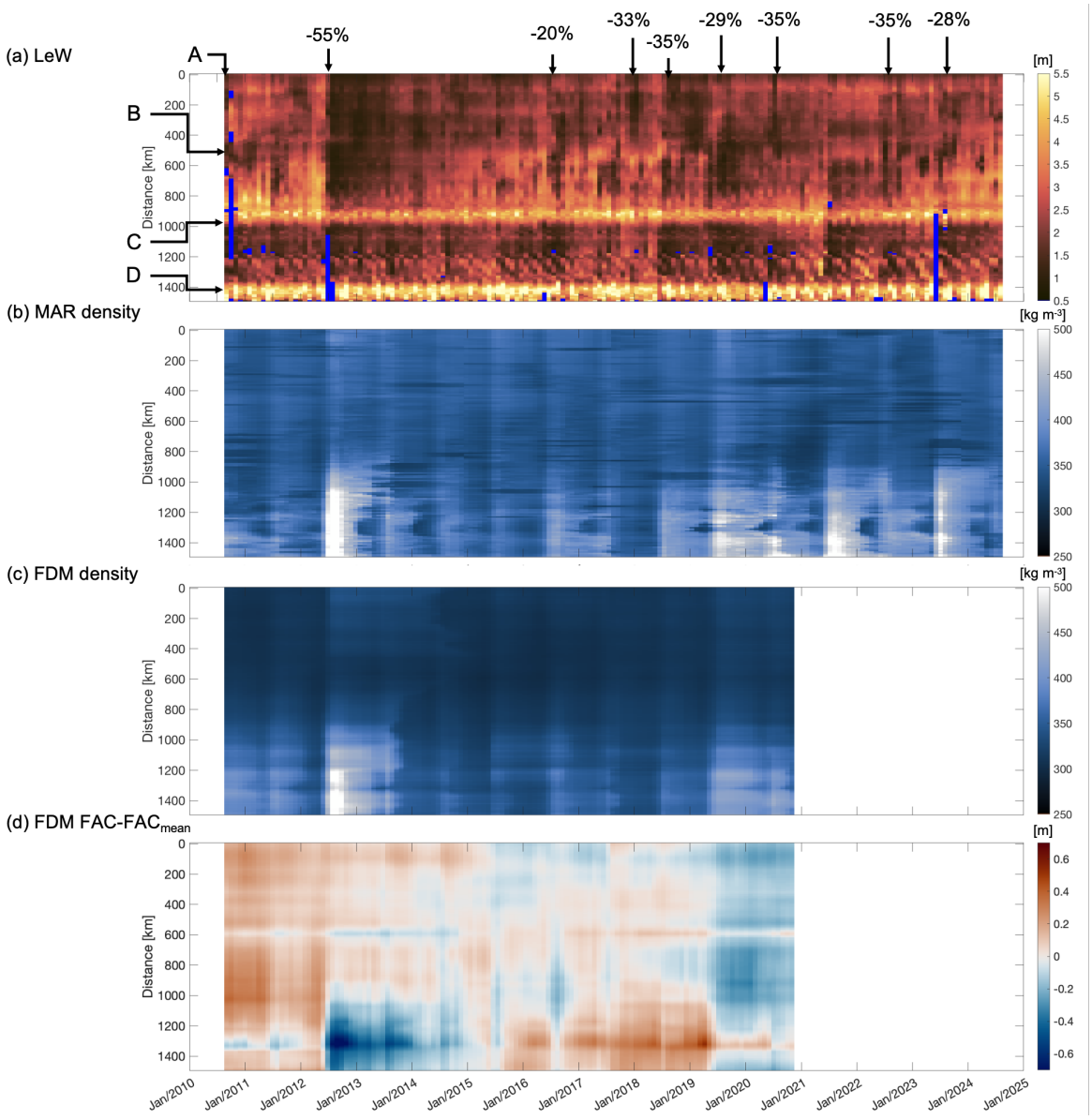

Figure A1. Monthly mean LeW, ~~daily~~ MAR ~~surface meltwater production~~density of the top 1.5 m of snow, ~~daily MAR meltwater refreezing~~IMAU-FDM density, and ~~daily accumulated total snow height change~~ IMAU-FDM firn air content (~~i.e. snow accumulation~~FAC) ~~from 12 July 2012~~ time series per pixel along the transect visualised in Fig. 1. The ~~LeW and MAR total snow height change~~ FAC time series ~~adopt a diverging colour bar~~ are normalised with respect to ~~enhance~~ the ~~contrast~~long-term mean of each pixel. The y-axes refer to the distance from the northernmost pixel. ~~White~~ Arrows indicate the inspected pixels A–D. Large LeW decreases with respect to the previous month for pixels north of pixel C are labelled. Blue (a) colour indicates the values that are not available.~~Arrows indicate the inspected pixels A—D.~~

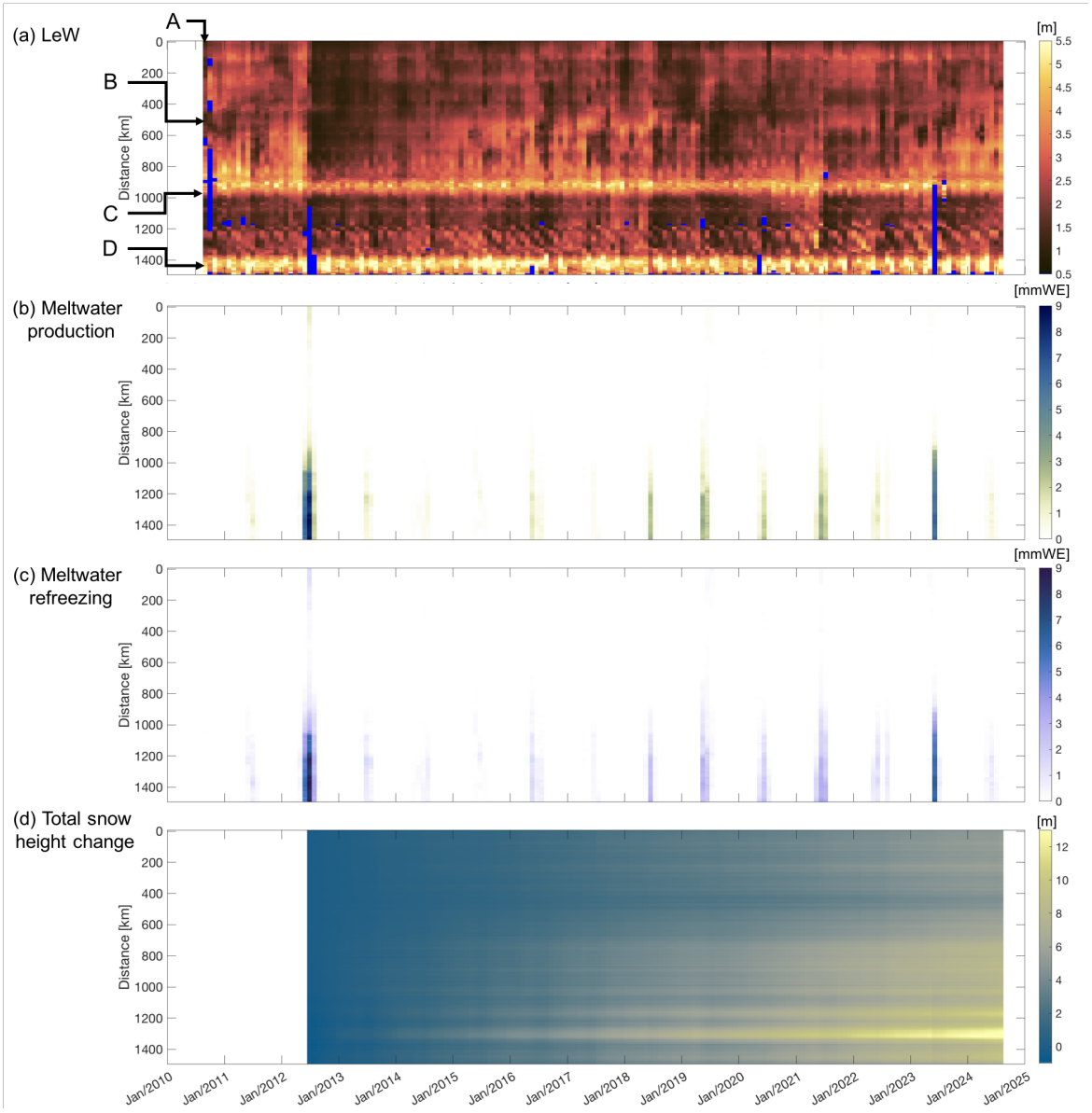

Figure A2. Monthly mean LeW, MAR surface meltwater production, MAR meltwater refreezing, and monthly accumulated total snow height change (i.e. snow accumulation) from 12 July 2012 time series per pixel along the transect visualised in Fig. 1. The y-axes refer to the distance from the northernmost pixel. White colour indicates the values that are not available. Arrows indicate the inspected pixels A—D.

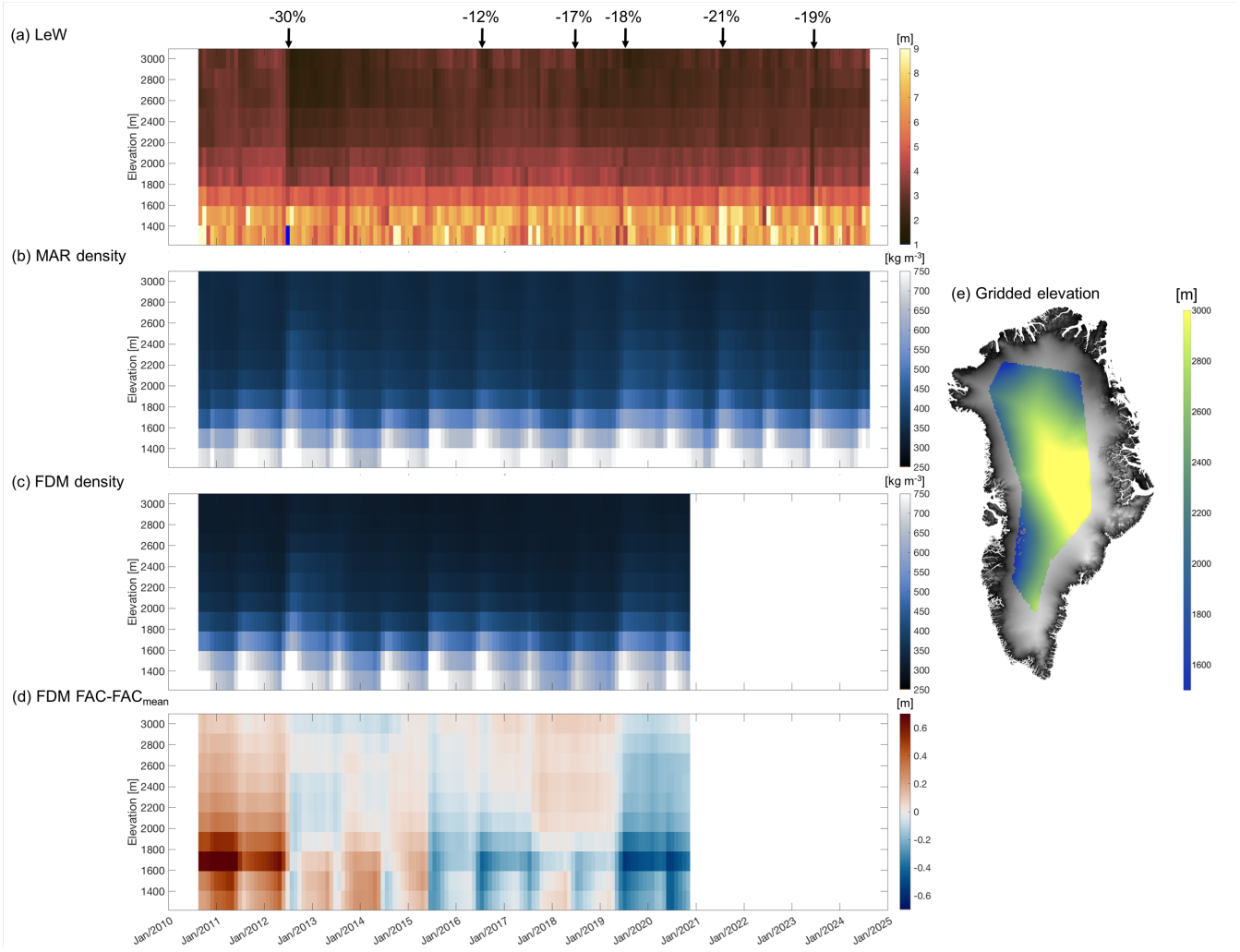

Figure A3. ~~Monthly~~ Time series of monthly mean LeW, ~~daily~~ density from MAR~~surface meltwater production~~, ~~daily meltwater refreezing~~density from IMAU-FDM, and ~~daily accumulated total snow height change (i.e. snow accumulation)~~ normalised FAC from ~~July 2012 time series~~ IMAU-FDM, grouped by a down-sampled (gridded) DEM. ~~The LeW and MAR total snow height change time series adopt a diverging colour bar to enhance the contrast. White colour indicates that the data are not available.~~ A map of the gridded DEM is provided on the right (e), with the original 1 km ×1 km ~~Helm et al. (2014b) DEM~~ ArcticDEM as background.

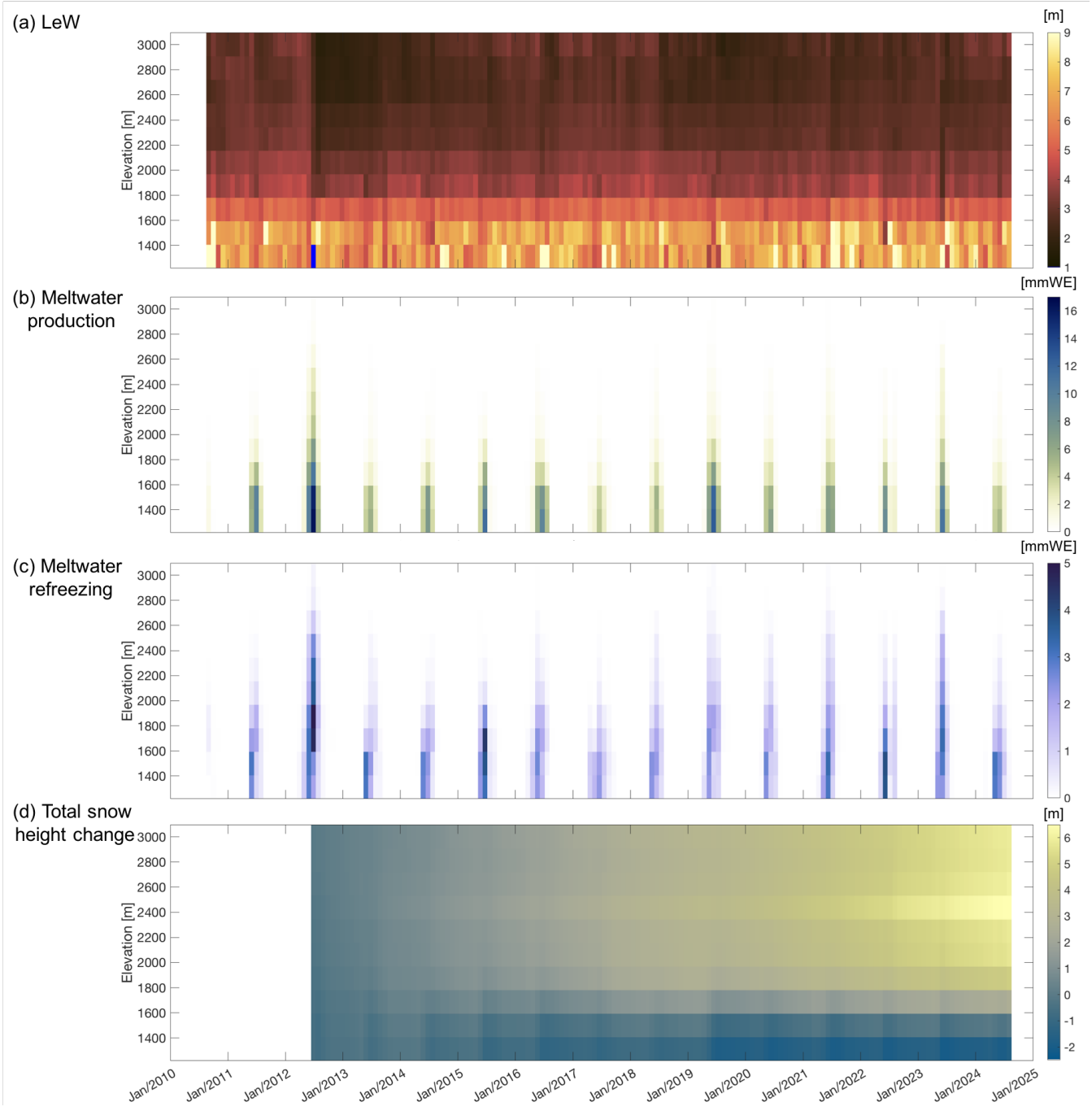

Figure A4. Monthly mean LeW, MAR surface meltwater production, meltwater refreezing, and monthly accumulated total snow height change (i.e. snow accumulation) from July 2012 time series grouped by a down-sampled (gridded) DEM. White colour indicates that the data are not available.

Acknowledgements. The research is supported by the Dutch Research Council (NWO) through the ALWGO.2017.033 project. ArcticDEM is provided by the Polar Geospatial Center under NSF-OPP awards 1043681, 1559691, and 1542736. ~~The DEM of Greenland used for result visualisation is provided by Helm et al. (2014a, b) under license Creative Commons Attribution 3.0 Unported.~~Some of the colour maps are acquired from Crameri (2023) under an MIT License.

ChatGPT is used for language checks in parts of the manuscript.

References

Abdalati, W., Zwally, H. J., Bindschadler, R., Csatho, B., Farrell, S. L., Fricker, H. A., Harding, D., Kwok, R., Lefsky, M., Markus, T., et al.: The ICESat-2 laser altimetry mission, Proceedings of the IEEE, 98, 735–751, 2010.

Adodo, F. I., Remy, F., and Picard, G.: Seasonal variations of the backscattering coefficient measured by radar altimeters over the Antarctic Ice Sheet, The Cryosphere, 12, 1767–1778, https://doi.org/10.5194/tc-12-1767-2018, 2018.

Alley, K., Scambos, T., Miller, J., Long, D., and MacFerrin, M.: Quantifying vulnerability of Antarctic ice shelves to hydrofracture using microwave scattering properties, Remote Sensing of Environment, 210, 297–306, https://doi.org/10.1016/j.rse.2018.03.025, 2018.

Bamber, J. L.: Ice sheet altimeter processing scheme, International Journal of Remote Sensing, 15, 925–938, https://doi.org/10.1080/01431169408954125, 1994.

Bermudez-Edo, M., Barnaghi, P., and Moessner, K.: Analysing real world data streams with spatio-temporal correlations: Entropy vs. Pearson correlation, Automation in Construction, 88, 87–100, https://doi.org/10.1016/j.autcon.2017.12.036, 2018.

Brils, M., Kuipers Munneke, P., van de Berg, W. J., and van den Broeke, M.: Improved representation of the contemporary Greenland ice sheet firn layer by IMAU-FDM v1.2G, Geoscientific Model Development, 15, 7121–7138, https://doi.org/10.5194/gmd-15-7121-2022, 2022.

Castelao, R. M. and Medeiros, P. M.: Coastal Summer Freshening and Meltwater Input off West Greenland from Satellite Observations, Remote Sensing, 14, 6069, https://doi.org/10.3390/rs14236069, 2022.

Crameri, F.: Scientific colour maps, https://doi.org/10.5281/ZENODO.1243862, 2023.

Davis, C.: A robust threshold retracking algorithm for measuring ice-sheet surface elevation change from satellite radar altimeters, IEEE Transactions on Geoscience and Remote Sensing, 35, 974–979, https://doi.org/10.1109/36.602540, 1997.

Davis, C. H. and Zwally, H. J.: Geographic and seasonal variations in the surface properties of the ice sheets by satellite-radar altimetry, Journal of Glaciology, 39, 687–697, https://doi.org/10.3189/S0022143000016580, 1993.

European Space Agency: L1b LRM Precise Orbit. Baseline D, https://doi.org/10.5270/CR2-cbow23i, (last access: 17 Semptember 2022), 2019.

Fahnestock, M., Bindschadler, R., Kwok, R., and Jezek, K.: Greenland Ice Sheet Surface Properties and Ice Dynamics from ERS-1 SAR Imagery, Science, 262, 1530–1534, https://doi.org/10.1126/science.262.5139.1530, 1993.

Fair, Z., Flanner, M., Neumann, T., Vuyovich, C., Smith, B., and Schneider, A.: Quantifying Volumetric Scattering Bias in ICESat-2 and Operation IceBridge Altimetry Over Greenland Firn and Aged Snow, Earth and Space Science, 11, https://doi.org/10.1029/2022ea002479, 2024.

Fettweis, X., Tedesco, M., van den Broeke, M., and Ettema, J.: Melting trends over the Greenland ice sheet (1958–2009) from spaceborne microwave data and regional climate models, The Cryosphere, 5, 359–375, https://doi.org/10.5194/tc-5-359-2011, 2011.

Fettweis, X., Box, J. E., Agosta, C., Amory, C., Kittel, C., Lang, C., van As, D., Machguth, H., and Gallée, H.: Reconstructions of the 1900–2015 Greenland ice sheet surface mass balance using the regional climate MAR model, The Cryosphere, 11, 1015–1033, https://doi.org/10.5194/tc-11-1015-2017, 2017.

Frappart, F., Blarel, F., Papa, F., Prigent, C., Mougin, E., Paillou, P., Baup, F., Zeiger, P., Salameh, E., Darrozes, J., Bourrel, L., and Rémy, F.: Backscattering signatures at Ka, Ku, C and S bands from low resolution radar altimetry over land, Advances in Space Research, 68, 989–1012, https://doi.org/10.1016/j.asr.2020.06.043, 2021.

Gardner, A. S., Schlegel, N.-J., and Larour, E.: Glacier Energy and Mass Balance (GEMB): a model of firn processes for cryosphere research, Geoscientific Model Development, 16, 2277–2302, https://doi.org/10.5194/gmd-16-2277-2023, 2023.

Gommenginger, C., Thibaut, P., Fenoglio-Marc, L., Quartly, G., Deng, X., Gómez-Enri, J., Challenor, P., and Gao, Y.: Retracking Altimeter Waveforms Near the Coasts, in: Coastal Altimetry, pp. 61–101, Springer Berlin Heidelberg, https://doi.org/10.1007/978-3-642-12796-0_4, 2010.

Grailet, J.-F., Hogan, R. J., Ghilain, N., Fettweis, X., and Grégoire, M.: Inclusion of the ECMWF ecRad radiation scheme (v1.5.0) in the MAR model (v3.14), regional evaluation for Belgium and assessment of surface shortwave spectral fluxes at Uccle observatory, EGUsphere [preprint], https://doi.org/10.5194/egusphere-2024-1858, 2024.

Hall, D., Box, J., Casey, K., Hook, S., Shuman, C., and Steffen, K.: Comparison of satellite-derived and in-situ observations of ice and snow surface temperatures over Greenland, Remote Sensing of Environment, 112, 3739–3749, https://doi.org/10.1016/j.rse.2008.05.007, 2008.

Harper, J., Humphrey, N., Pfeffer, W. T., Brown, J., and Fettweis, X.: Greenland ice-sheet contribution to sea-level rise buffered by meltwater storage in firn, Nature, 491, 240–243, https://doi.org/10.1038/nature11566, 2012.

Heilig, A., Eisen, O., MacFerrin, M., Tedesco, M., and Fettweis, X.: Seasonal monitoring of melt and accumulation within the deep percolation zone of the Greenland Ice Sheet and comparison with simulations of regional climate modeling, The Cryosphere, 12, 1851–1866, https://doi.org/10.5194/tc-12-1851-2018, 2018.

Helm, V., Humbert, A., and Miller, H.: Elevation and elevation change of Greenland and Antarctica derived from CryoSat-2, The Cryosphere, 8, 1539–1559, https://doi.org/10.5194/tc-8-1539-2014, 2014a.

Helm, V., Humbert, A., and Miller, H.: Elevation Model of Greenland derived from CryoSat-2 in the period 2011 to 2013, links to DEM and uncertainty map as GeoTIFF, https://doi.org/10.1594/PANGAEA.831393, 2014b.

Huybrechts, P., Goelzer, H., Janssens, I., Driesschaert, E., Fichefet, T., Goosse, H., and Loutre, M.-F.: Response of the Greenland and Antarctic Ice Sheets to Multi-Millennial Greenhouse Warming in the Earth System Model of Intermediate Complexity LOVECLIM, Surveys in Geophysics, 32, 397–416, https://doi.org/10.1007/s10712-011-9131-5, 2011.

Kern, M., Cullen, R., Berruti, B., Bouffard, J., Casal, T., Drinkwater, M. R., Gabriele, A., Lecuyot, A., Ludwig, M., Midthassel, R., Navas Traver, I., Parrinello, T., Ressler, G., Andersson, E., Martin-Puig, C., Andersen, O., Bartsch, A., Farrell, S., Fleury, S., Gascoin, S., Guillot, A., Humbert, A., Rinne, E., Shepherd, A., van den Broeke, M. R., and Yackel, J.: The Copernicus Polar Ice and Snow Topography Altimeter (CRISTAL) high-priority candidate mission, The Cryosphere, 14, 2235–2251, https://doi.org/10.5194/tc-14-2235-2020, 2020.

Koenig, L. S., Ivanoff, A., Alexander, P. M., MacGregor, J. A., Fettweis, X., Panzer, B., Paden, J. D., Forster, R. R., Das, I., McConnell, J. R., Tedesco, M., Leuschen, C., and Gogineni, P.: Annual Greenland accumulation rates (2009–2012) from airborne snow radar, The Cryosphere, 10, 1739–1752, https://doi.org/10.5194/tc-10-1739-2016, 2016.

Kuipers Munneke, P., Ligtenberg, S. R., Suder, E. A., and Van den Broeke, M. R.: A model study of the response of dry and wet firn to climate change, Annals of Glaciology, 56, 1–8, https://doi.org/10.3189/2015aog70a994, 2015.

Lacroix, P., Dechambre, M., Legrésy, B., Blarel, F., and Rémy, F.: On the use of the dual-frequency ENVISAT altimeter to determine snowpack properties of the Antarctic ice sheet, Remote Sensing of Environment, 112, 1712–1729, https://doi.org/10.1016/j.rse.2007.08.022, 2008.

Lambin, C., Fettweis, X., Kittel, C., Fonder, M., and Ernst, D.: Assessment of future wind speed and wind power changes over South Greenland using the Modèle Atmosphérique Régional regional climate model, International Journal of Climatology, 43, 558–574, https://doi.org/10.1002/joc.7795, 2022.

Larue, F., Picard, G., Aublanc, J., Arnaud, L., Robledano-Perez, A., Meur, E. L., Favier, V., Jourdain, B., Savarino, J., and Thibaut, P.: Radar altimeter waveform simulations in Antarctica with the Snow Microwave Radiative Transfer Model (SMRT), Remote Sensing of Environment, 263, 112 534, https://doi.org/10.1016/j.rse.2021.112534, 2021.

Legrésy, B. and Rémy, F.: Altimetric observations of surface characteristics of the Antarctic ice sheet, Journal of Glaciology, 43, 265–275, https://doi.org/10.3189/s002214300000321x, 1997.

Lenton, T. M., Held, H., Kriegler, E., Hall, J. W., Lucht, W., Rahmstorf, S., and Schellnhuber, H. J.: Tipping elements in the Earth's climate system, Proceedings of the National Academy of Sciences, 105, 1786–1793, https://doi.org/10.1073/pnas.0705414105, 2008.

Lewis, G., Osterberg, E., Hawley, R., Marshall, H. P., Meehan, T., Graeter, K., McCarthy, F., Overly, T., Thundercloud, Z., and Ferris, D.: Recent precipitation decrease across the western Greenland ice sheet percolation zone, The Cryosphere, 13, 2797–2815, https://doi.org/10.5194/tc-13-2797-2019, 2019.

Li, W., Slobbe, C., and Lhermitte, S.: A leading-edge-based method for correction of slope-induced errors in ice-sheet heights derived from radar altimetry, The Cryosphere, 16, 2225–2243, https://doi.org/10.5194/tc-16-2225-2022, 2022.

MacFerrin, M. J., Stevens, C. M., Vandecrux, B., Waddington, E. D., and Abdalati, W.: The Greenland Firn Compaction Verification and Reconnaissance (FirnCover) dataset, 2013–2019, Earth System Science Data, 14, 955–971, https://doi.org/10.5194/essd-14-955-2022, 2022.

Machguth, H., MacFerrin, M., van As, D., Box, J. E., Charalampidis, C., Colgan, W., Fausto, R. S., Meijer, H. A. J., Mosley-Thompson, E., and van de Wal, R. S. W.: Greenland meltwater storage in firn limited by near-surface ice formation, Nature Climate Change, 6, 390–393, https://doi.org/10.1038/nclimate2899, 2016.

Machguth, H., Tedstone, A., Kuipers Munneke, P., Brils, M., Noël, B., Clerx, N., Jullien, N., Fettweis, X., and van den Broeke, M.: Runoff from Greenland's firn area – why do MODIS, RCMs and a firn model disagree?, EGUsphere [preprint], https://doi.org/10.5194/egusphere-2024-2750, 2024.

Medley, B., Neumann, T. A., Zwally, H. J., Smith, B. E., and Stevens, C. M.: Simulations of firn processes over the Greenland and Antarctic ice sheets: 1980–2021, The Cryosphere, 16, 3971–4011, https://doi.org/10.5194/tc-16-3971-2022, 2022.

Meierbachtol, T., Harper, J., and Humphrey, N.: Basal Drainage System Response to Increasing Surface Melt on the Greenland Ice Sheet, Science, 341, 777–779, https://doi.org/10.1126/science.1235905, 2013.

Meloni, M., Bouffard, J., Parrinello, T., Dawson, G., Garnier, F., Helm, V., Bella, A. D., Hendricks, S., Ricker, R., Webb, E., Wright, B., Nielsen, K., Lee, S., Passaro, M., Scagliola, M., Simonsen, S. B., Sørensen, L. S., Brockley, D., Baker, S., Fleury, S., Bamber, J., Maestri, L., Skourup, H., Forsberg, R., and Mizzi, L.: CryoSat Ice Baseline-D validation and evolutions, The Cryosphere, 14, 1889–1907, https://doi.org/10.5194/tc-14-1889-2020, 2020.

Michel, A., Flament, T., and Rémy, F.: Study of the Penetration Bias of ENVISAT Altimeter Observations over Antarctica in Comparison to ICESat Observations, Remote Sensing, 6, 9412–9434, https://doi.org/10.3390/rs6109412, 2014.

National Snow and Ice Data Center (NSIDC): ATL06 release 005 known issues, https://nsidc.org/sites/nsidc.org/files/technical-references/ICESat2_ATL06_Known_Issues_v005.pdf, [Date accessed: 18 April, 2022], 2021.

Nghiem, S. V., Hall, D. K., Mote, T. L., Tedesco, M., Albert, M. R., Keegan, K., Shuman, C. A., DiGirolamo, N. E., and Neumann, G.: The extreme melt across the Greenland ice sheet in 2012, Geophysical Research Letters, 39, https://doi.org/10.1029/2012gl053611, 2012.

Nilsson, J., Vallelonga, P., Simonsen, S. B., Sørensen, L. S., Forsberg, R., Dahl-Jensen, D., Hirabayashi, M., Goto-Azuma, K., Hvidberg, C. S., Kjaer, H. A., and Satow, K.: Greenland 2012 melt event effects on CryoSat-2 radar altimetry, Geophysical Research Letters, 42, 3919–3926, https://doi.org/10.1002/2015gl063296, 2015.

Noh, M.-J. and Howat, I. M.: Automated stereo-photogrammetric DEM generation at high latitudes: Surface Extraction with TIN-based Search-space Minimization (SETSM) validation and demonstration over glaciated regions, GIScience & Remote Sensing, 52, 198–217, https://doi.org/10.1080/15481603.2015.1008621, 2015.

Noël, B., van de Berg, W. J., van Wessem, J. M., van Meijgaard, E., van As, D., Lenaerts, J. T. M., Lhermitte, S., Kuipers Munneke, P., Smeets, C. J. P. P., van Ulft, L. H., van de Wal, R. S. W., and van den Broeke, M. R.: Modelling the climate and surface mass balance of polar ice sheets using RACMO2 – Part 1: Greenland (1958–2016), The Cryosphere, 12, 811–831, https://doi.org/10.5194/tc-12-811-2018, 2018.

Otosaka, I. N.: Firn density profiles in West Central Greenland (ESA CryoVEx 2017), https://doi.org/10.1594/PANGAEA.921672, (last access: 27 October 2023), 2020.

Otosaka, I. N., Shepherd, A., Casal, T. G. D., Coccia, A., Davidson, M., Di Bella, A., Fettweis, X., Forsberg, R., Helm, V., Hogg, A. E., Hvidegaard, S. M., Lemos, A., Macedo, K., Kuipers Munneke, P., Parrinello, T., Simonsen, S. B., Skourup, H., and Sørensen, L. S.: Surface Melting Drives Fluctuations in Airborne Radar Penetration in West Central Greenland, Geophysical Research Letters, 47, https://doi.org/10.1029/2020gl088293, 2020.

Porter, C., Howat, I., Noh, M.-J., Husby, E., Khuvis, S., Danish, E., Tomko, K., Gardiner, J., Negrete, A., Yadav, B., Klassen, J., Kelleher, C., Cloutier, M., Bakker, J., Enos, J., Arnold, G., Bauer, G., and Morin, P.: ArcticDEM - Mosaics, Version 4.1, https://doi.org/10.7910/DVN/3VDC4W, 2023.

Rennermalm, Å. K., Hock, R., Covi, F., Xiao, J., Corti, G., Kingslake, J., Leidman, S. Z., Miège, C., Macferrin, M., Machguth, H., Osterberg, E., Kameda, T., and McConnell, J. R.: Shallow firn cores 1989–2019 in southwest Greenland's percolation zone reveal decreasing density and ice layer thickness after 2012, Journal of Glaciology, 68, 431–442, https://doi.org/10.1017/jog.2021.102, 2021.

Ridley, J. K. and Partington, K. C.: A model of satellite radar altimeter return from ice sheets, International Journal of Remote Sensing, 9, 601–624, https://doi.org/10.1080/01431168808954881, 1988.

Rinne, E. and Similä, M.: Utilisation of CryoSat-2 SAR altimeter in operational ice charting, The Cryosphere, 10, 121–131, https://doi.org/10.5194/tc-10-121-2016, 2016.

Ronan, A. C., Hawley, R. L., and Chipman, J. W.: Impacts of differing melt regimes on satellite radar waveforms and elevation retrievals, The Cryosphere, 18, 5673–5683, https://doi.org/10.5194/tc-18-5673-2024, 2024.

Rutishauser, A., Scanlan, K. M., Vandecrux, B., Karlsson, N. B., Jullien, N., Ahlstrøm, A. P., Fausto, R. S., and How, P.: Mapping the vertical heterogeneity of Greenland's firn from 2011–2019 using airborne radar and laser altimetry, The Cryosphere, 18, 2455–2472, https://doi.org/10.5194/tc-18-2455-2024, 2024.

Sasgen, I., van den Broeke, M., Bamber, J. L., Rignot, E., Sørensen, L. S., Wouters, B., Martinec, Z., Velicogna, I., and Simonsen, S. B.: Timing and origin of recent regional ice-mass loss in Greenland, Earth and Planetary Science Letters, 333-334, 293–303, https://doi.org/10.1016/j.epsl.2012.03.033, 2012.

Scanlan, K. M., Rutishauser, A., and Simonsen, S. B.: Observing the Near-Surface Properties of the Greenland Ice Sheet, Geophysical Research Letters, 50, https://doi.org/10.1029/2022gl101702, 2023.

Schaller, C. F., Freitag, J., Kipfstuhl, S., Laepple, T., Steen-Larsen, H. C., and Eisen, O.: A representative density profile of the North Greenland snowpack, The Cryosphere, 10, 1991–2002, https://doi.org/10.5194/tc-10-1991-2016, 2016a.

Schaller, C. F., Freitag, J., Kipfstuhl, S., Laepple, T., Steen-Larsen, H. C., and Eisen, O.: NEEM to EGRIP traverse - density and δ^{18}O of the surface snow (2 m profiles), https://doi.org/10.1594/PANGAEA.867875, (last access: 13 December 2023), 2016b.

Simonsen, S. B. and Sørensen, L. S.: Implications of changing scattering properties on Greenland ice sheet volume change from Cryosat-2 altimetry, Remote Sensing of Environment, 190, 207–216, https://doi.org/10.1016/j.rse.2016.12.012, 2017.

Slater, T., Shepherd, A., McMillan, M., Muir, A., Gilbert, L., Hogg, A. E., Konrad, H., and Parrinello, T.: A new digital elevation model of Antarctica derived from CryoSat-2 altimetry, The Cryosphere, 12, 1551–1562, https://doi.org/10.5194/tc-12-1551-2018, 2018.

Slater, T., Shepherd, A., Mcmillan, M., Armitage, T. W. K., Otosaka, I., and Arthern, R. J.: Compensating Changes in the Penetration Depth of Pulse-Limited Radar Altimetry Over the Greenland Ice Sheet, IEEE Transactions on Geoscience and Remote Sensing, 57, 9633–9642, https://doi.org/10.1109/tgrs.2019.2928232, 2019.

Smith, B., Fricker, H. A., Gardner, A., Siegfried, M. R., Adusumilli, S., Csathó, B. M., Holschuh, N., Nilsson, J., Paolo, F. S., and the ICESat-2 Science Team: ATLAS/ICESat-2 L3A Land Ice Height, Version 5, https://doi.org/10.5067/ATLAS/ATL06.005, (last access: 15 Semptember 2022), 2020.

Smith, B., H. A. Fricker, A. Gardner, M. R. Siegfried, S. Adusumilli, B. M. Csath??, N. Holschuh, J. Nilsson, F. S. Paolo, and Team, T. I.-. S.: ATLAS/ICESat-2 L3A Land Ice Height, Version 6, https://doi.org/10.5067/ATLAS/ATL06.006, (Date Accessed: 7 February 2025), 2023a.

Smith, B., Hancock, D., Harbeck, K., Roberts, L., Neumann, T., Brunt, K., Fricker, H., Gardner, A., Siegfried, M., Adusumilli, S., Csatho, B., Holschuh, N., Nilsson, J., Paolo, F., and Felikson, D.: Ice, Cloud, and Land Elevation Satellite (ICESat-2) Project Algorithm Theoretical Basis Document (ATBD) for Land Ice Along-Track Height Product (ATL06), version 6, https://doi.org/10.5067/VWOKQDYJ7ODB, 2023b.

Smith, B. E., Gardner, A., Schneider, A., and Flanner, M.: Modeling biases in laser-altimetry measurements caused by scattering of green light in snow, Remote Sensing of Environment, 215, 398–410, https://doi.org/10.1016/j.rse.2018.06.012, 2018.

Smith, B. E., Medley, B., Fettweis, X., Sutterley, T., Alexander, P., Porter, D., and Tedesco, M.: Evaluating Greenland surface-mass-balance and firn-densification data using ICESat-2 altimetry, The Cryosphere, 17, 789–808, https://doi.org/10.5194/tc-17-789-2023, 2023c.

Sundal, A. V., Shepherd, A., Nienow, P., Hanna, E., Palmer, S., and Huybrechts, P.: Melt-induced speed-up of Greenland ice sheet offset by efficient subglacial drainage, Nature, 469, 521–524, https://doi.org/10.1038/nature09740, 2011.

Tedesco, M. and Fettweis, X.: Unprecedented atmospheric conditions (1948–2019) drive the 2019 exceptional melting season over the Greenland ice sheet, The Cryosphere, 14, 1209–1223, https://doi.org/10.5194/tc-14-1209-2020, 2020.

Tedesco, M., Fettweis, X., van den Broeke, M. R., van de Wal, R. S. W., Smeets, C. J. P. P., van de Berg, W. J., Serreze, M. C., and Box, J. E.: The role of albedo and accumulation in the 2010 melting record in Greenland, Environmental Research Letters, 6, 014 005, https://doi.org/10.1088/1748-9326/6/1/014005, 2011.

Tedesco, M., Fettweis, X., Mote, T., Wahr, J., Alexander, P., Box, J. E., and Wouters, B.: Evidence and analysis of 2012 Greenland records from spaceborne observations, a regional climate model and reanalysis data, The Cryosphere, 7, 615–630, https://doi.org/10.5194/tc-7-615-2013, 2013.

Tedesco, M., Mote, T., Fettweis, X., Hanna, E., Jeyaratnam, J., Booth, J. F., Datta, R., and Briggs, K.: Arctic cut-off high drives the poleward shift of a new Greenland melting record, Nature Communications, 7, https://doi.org/10.1038/ncomms11723, 2016.

Trusel, L. D., Das, S. B., Osman, M. B., Evans, M. J., Smith, B. E., Fettweis, X., McConnell, J. R., Noël, B. P. Y., and van den Broeke, M. R.: Nonlinear rise in Greenland runoff in response to post-industrial Arctic warming, Nature, 564, 104–108, https://doi.org/10.1038/s41586-018-0752-4, 2018.

van den Broeke, M. R., Enderlin, E. M., Howat, I. M., Munneke, P. K., Noël, B. P. Y., van de Berg, W. J., van Meijgaard, E., and Wouters, B.: On the recent contribution of the Greenland ice sheet to sea level change, The Cryosphere, 10, 1933–1946, https://doi.org/10.5194/tc-10-1933-2016, 2016.

van den Broeke, M. R., Kuipers Munneke, P., Noël, B., Reijmer, C., Smeets, P., van de Berg, W. J., and van Wessem, J. M.: Contrasting current and future surface melt rates on the ice sheets of Greenland and Antarctica: Lessons from in situ observations and climate models, PLOS Climate, 2, e0000 203, https://doi.org/10.1371/journal.pclm.0000203, 2023.

Vandecrux, B., MacFerrin, M., Machguth, H., Colgan, W. T., van As, D., Heilig, A., Stevens, C. M., Charalampidis, C., Fausto, R. S., Morris, E. M., Mosley-Thompson, E., Koenig, L., Montgomery, L. N., Miège, C., Simonsen, S. B., Ingeman-Nielsen, T., and Box, J. E.: Firn data compilation reveals widespread decrease of firn air content in western Greenland, The Cryosphere, 13, 845–859, https://doi.org/10.5194/tc-13-845-2019, 2019.

Vandecrux, B., Box, J., Ahlstrøm, A., Fausto, R., Karlsson, N., Rutishauser, A., Citterio, M., Larsen, S., Heuer, J., Solgaard, A., How, P., Colgan, W., and Fahrner, D.: GEUS snow and firn data in Greenland, https://doi.org/10.22008/FK2/9QEOWZ, 2023.

Vandecrux, B., Amory, C., Ahlstrøm, A. P., Akers, P. D., Albert, M., Alley, R. B., Alves De Castro, M., Arnaud, L., Baker, I., Bales, R., Benson, C., Box, J. E., Brucker, L., Buizert, C., Chandler, D., Charalampidis, C., Cherblanc, C., Clerx, N., Colgan, W., Covi, F., Dattler, M., Denis, G., Derksen, C., Dibb, J. E., Ding, M., Dixon, D., Eisen, O., Fahrner, D., Fausto, R., Favier, V., Fernandoy, F., Freitag, J., Gerland, S., Harper, J., Hawley, R. L., Heuer, J., Hock, R., Hou, S., How, P., Humphrey, N., Hubbard, B., Iizuka, Y., Isaksson, E., Kameda, T., Karlsson, N. B., Kawakami, K., Kjær, H. A., Kreutz, K., Kuipers Munneke, P., Lazzara, M., Lemeur, E., Lenaerts, J. T. M., Lewis, G., Lindau, F. G. L., Lindsey-Clark, J., MacFerrin, M., Machguth, H., Magand, O., Mankoff, K. D., Marquetto, L., Martinerie, P., McConnell, J. R., Medley, B., Miège, C., Miles, K. E., Miller, O., Miller, H., Montgomery, L., Morris, E., Mosley-Thompson, E., Mulvaney, R., Niwano, M., Oerter, H., Osterberg, E., Otosaka, I., Picard, G., Polashenski, C., Reijmer, C., Rennermalm, A., Rutishauser, A., Scanlan, K., Simoes, J. C., Simonsen, S. B., Smeets, P. C., Smith, A., Solgaard, A., Spencer, M., Steen-Larsen, H. C., Stevens, C. M., Sugiyama, S., Svensson, J., Tedesco, M., Thomas, E., Thompson-Munson, M., Tsutaki, S., Van As, D., Van Den Broeke, M. R., Van Tiggelen, M., Wang, Y., Wilhelms, F., Winstrup, M., Xiao, J., and Xiao, C.: The SUMup collaborative database: Surface mass balance, subsurface temperature and density measurements from the Greenland and Antarctic ice sheets (2024 release), https://doi.org/10.18739/A2M61BR5M, 2024.

Vizcaíno, M., Mikolajewicz, U., Jungclaus, J., and Schurgers, G.: Climate modification by future ice sheet changes and consequences for ice sheet mass balance, Climate Dynamics, 34, 301–324, https://doi.org/10.1007/s00382-009-0591-y, 2009.

Wingham, D., Rapley, C., and D, G.: New Techniques in Satellite Altimeter Tracking Systems, in: Digest - International Geoscience and Remote Sensing Symposium (IGARSS), vol. ESA SP-254, pp. 1339–1344, Zurich, 1986.

Wingham, D., Francis, C., Baker, S., Bouzinac, C., Brockley, D., Cullen, R., de Chateau-Thierry, P., Laxon, S., Mallow, U., Mavrocordatos, C., Phalippou, L., Ratier, G., Rey, L., Rostan, F., Viau, P., and Wallis, D.: CryoSat: A mission to determine the fluctuations in Earth's land and marine ice fields, Advances in Space Research, 37, 841–871, https://doi.org/https://doi.org/10.1016/j.asr.2005.07.027, natural Hazards and Oceanographic Processes from Satellite Data, 2006.

Węglarczyk, S.: Kernel density estimation and its application, ITM Web of Conferences, 23, 00 037, https://doi.org/10.1051/itmconf/20182300037, 2018.

Zwally, H. J., Abdalati, W., Herring, T., Larson, K., Saba, J., and Steffen, K.: Surface Melt-Induced Acceleration of Greenland Ice-Sheet Flow, Science, 297, 218–222, https://doi.org/10.1126/science.1072708, 2002.